Progress in Oceanography 234 (2025) 103466

Contents lists available at ScienceDirect

Progress in Oceanography

journal homepage: www.elsevier.com/locate/pocean

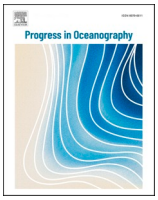

Surface CO_2 partial pressure and air–sea CO_2 flux on the China side of the South Yellow Sea based on multiple-year underway measurements during 2005–2011 and comparison with results for 2011–2018

Wei-dong Zhai [a,*], Xiang-hui Guo [b], Yan Bai [c], Xianqiang He [c], Kai Tang [b], Minhan Dai [b]

[a] Frontier Research Center, Southern Marine Science and Engineering Guangdong Laboratory (Zhuhai), Zhuhai 519082, China
[b] State Key Laboratory of Marine Environmental Science, and College of Ocean and Earth Sciences, Xiamen University, Xiamen 361102, China
[c] State Key Laboratory of Satellite Ocean Environment Dynamics, Second Institute of Oceanography, Ministry of Natural Resources, Hangzhou 310012, China

A B S T R A C T

By resolving spatiotemporal variations in sea surface partial pressure of CO_2 (pCO_2) based on multiple-year underway measurements, we quantified basin-scale air–sea CO_2 exchange flux on the China side of the South Yellow Sea between 2005 and 2011, and compared it with the result obtained between 2011 and 2018. Over the three subregions under study, the area-weighted average of the CO_2 influx rate was estimated to be 1.1 ± 1.5 mol m^{-2} yr^{-1} during 2005–2011, which is only half the annual CO_2 influx rate over the adjacent East China Sea shelf but not remarkably different from the rate (0.4 ± 2.1 mol m^{-2} yr^{-1}) estimated for almost the same sea area during 2011–2018. Over central and western parts of the South Yellow Sea, subregion-specific fitting curves of monthly variations in air–sea CO_2 flux during 2005–2011 were consistent with those monthly variations during 2011–2018. However, over the southern part of the South Yellow Sea near the Changjiang Estuary, the fitting curve of monthly variations in air–sea CO_2 fluxes during 2005–2011 located systematically on one side of the monthly variation estimated for 2011–2018, indicating that annual CO_2 uptake had weakened in this subregion. Both cases were different from some other ocean margin areas characterized by enhanced CO_2 uptake following rise in atmospheric CO_2. To study the potential shift in terms of shelf CO_2 sources and sinks over multiple decades and under environmental changes, further field observations and data-based research are needed on several large continental shelves.

1. Introduction

Despite comprising just 7–8 % of the world's ocean surface area, continental shelf seas play a nonnegligible role in the global oceanic uptake of atmospheric CO_2 (e.g., Wanninkhof et al., 2013; Laruelle et al., 2014; Dai et al., 2022). Recent evidence has shown that the CO_2 influx rate of some continental shelf systems might have increased during the past several decades (Laruelle et al., 2018; Mathis et al., 2024). However, quantifying air–sea CO_2 fluxes on continental shelves and understanding their variations remain challenging (Resplandy et al., 2024) because coastal waters are highly heterogeneous in terms of air–sea CO_2 exchange (Laruelle et al., 2010; Cai, 2011; Chen et al., 2013; Dai et al., 2013; 2022). Moreover, continental shelves are affected by intense human disturbances such as sewage discharges and coastal wetland reclamation (Bauer et al., 2013; Regnier et al., 2013; Li et al., 2023a).

The East China Sea (ECS) and the South Yellow Sea (SYS) together represent a globally important shelf system, characterized by a wide shelf and water exchange between complex coastal currents and the Kuroshio Current system (Fig. 1). The ECS serves as a remarkable annual net sink of atmospheric CO_2 (Zhang et al., 1997; Tsunogai et al., 1999; Tseng et al., 2014; Guo et al., 2015), whereas the SYS serves as a weak annual sink of atmospheric CO_2 (Choi et al., 2019; Wang and Zhai, 2021; Ko et al., 2022). In 2023, Li et al. (2023b) applied a random-forest-algorithm-based machine learning method to modeling of the surface partial pressure of CO_2 (pCO_2) in the Yellow Sea, using Moderate Resolution Imaging Spectroradiometer (MODIS) derived sea surface temperature, chlorophyll-a concentration, diffuse attenuation of downwelling irradiance, and salinity. Their modeled pCO_2 increased at a rate much slower than the rate of increase in atmospheric CO_2, implying that the Yellow Sea might have changed from an annual source of atmospheric CO_2 in the 2000 s to an annual sink in the 2010 s (Li et al., 2023b). However, the correctness of machine learning methods is highly subject to the training datasets used, and Li et al. (2023b) trained their model using only a dataset obtained between 2011 and 2019, thereby lacking verification through the 2000 s. By contrast, another satellite retrieval algorithm (combining a semi-mechanistic algorithm and machine learning method) indicated that the rate of increase in Yellow Sea pCO_2 during 2003–2019 should be close to that of the rise in atmospheric CO_2 (Yu et al., 2023). To examine the reliability of those machine learning results, further investigation of additional field data is

* Corresponding author.
E-mail addresses: zhaiweidong@sml-zhuhai.cn, wdzhai@126.com (W.-d. Zhai).

https://doi.org/10.1016/j.pocean.2025.103466
Received 13 June 2024; Received in revised form 19 February 2025; Accepted 13 March 2025
Available online 16 March 2025

needed.

Between 2005 and 2011, we conducted 26 cruises through combined areas of the ECS and the SYS (Supplementary Table S1), obtaining underway measurements of sea surface pCO_2 (Supplementary Fig. S1). Most of those cruises passed through two or three of the three physical–biogeochemical domains in the SYS categorized in the present study (Table 1). Although Zhai and Dai (2009) and Guo et al. (2015) both used some data other than those obtained in September 2008, June 2009, and November/December 2011, they focused on the air–sea CO_2 exchange in the ECS and largely ignored those data obtained in the SYS. In this study, we revisited this dataset and elucidated the seasonal or even monthly variations in air–sea CO_2 flux in the SYS between 2005 and 2011 based on underway pCO_2 measurements. We then compared our results with the data published by Wang and Zhai (2021), who reported monthly variations in air–sea CO_2 flux over the same shelf region between 2011 and 2018. The objective of this study was to conduct a trend analysis of air–sea CO_2 flux in the Yellow Sea, an important continental shelf sea, using the available datasets. To avoid potential confusion induced by zoning overlapping between this study and Guo et al. (2015), we also recalculated results for the ECS shelf (see Supplementary Materials), based on a slightly updated zoning scheme from Guo et al. (2015) over the ECS region (Fig. 1C, Supplementary Table S2).

2. Materials and methods

During the cruises, temperature and salinity of the pumped surface seawater were measured continuously using either a YSI 6600 meter (Yellow Springs Instrument Co., U.S.) or a set of Idronaut Multiparameter "Flow Through" sensor modules (IDRONAUT S.r.l., Italy). All salinity data were corrected to the practical salinity scale 1978, while sea surface temperature (SST) and dissolved oxygen (DO) were corrected on the basis of intercomparison experiments between underway pumping measurements and vertical profile measurements at sampling stations. For pCO_2 determination, a Li-Cor® nondispersive infrared spectrometer (Li-7000) was used to measure the dried CO_2 fraction (xCO_2) in the equilibrator and in the air. For calibration purposes, CO_2 gas standards with xCO_2 values in the range of 138–967 ppmv (parts per million by volume in dry air) were applied. The pCO_2 data was transformed from corrected xCO_2 based on either barometric pressure along the transect or air pressure in the Li-7000 detector. Intercalibration testing showed that both air pressure data sets were consistent at a relative error level of < 0.3 % (i.e., < 3 hPa). The Weiss and Price (1980) saturated water vapor pressure and the Takahashi et al. (1993) temperature effect coefficient of 4.23 % $°C^{-1}$ were used to calculate in situ sea surface pCO_2. The overall uncertainty of the xCO_2 measurements and the pCO_2 data processing was < 1 % (Zhai and Dai, 2009).

Considering the complexity of the geographical features and the hydrological conditions in coastal seas (Guo et al., 2015; Wang and Zhai, 2021), the study area of the SYS was divided into three subregions: (I) the western SYS, (II) the Chinese side of the central SYS, and (III) the southern part of the SYS (Fig. 1C, Table 1). The western SYS is characterized by the Jiangsu Shallows and the resuspension of local sediments. The boundary between the western and central SYS areas is aligned approximately along the Jiangsu Front and the Shandong Peninsula Front in winter (Chen, 2009). The southern SYS, which is confined to the region south of 34°N, is affected by the Changjiang Diluted Water in summer (Chen, 2009; Guo et al., 2015). In this study, we assumed that the arithmetic mean of the field data was representative of the given subregion during the survey.

The flux calculation was based on the formula $F = k \times K_H \times \Delta pCO_2$, where k is the gas transfer velocity of CO_2, K_H is the solubility of CO_2 in seawater (Weiss, 1974), and ΔpCO_2 is the mean sea-to-air pCO_2 difference. A positive flux value represented net CO_2 exchange from the sea to the atmosphere, whereas a negative flux value represented net CO_2 exchange from the atmosphere to the sea. Because in situ measurements of atmospheric CO_2 concentration were not always available during our surveys, we calculated the air-equilibrated pCO_2 levels based on flask analysis data of the atmospheric CO_2 mole fraction at the adjacent Taeahn Peninsula site (36°44′N, 126°08′E), which is located to the west of South Korea (data from the U.S. NOAA/ESRL's Global Monitoring Division, https://www.esrl.noaa.gov/gmd/), and corrected them to survey-based barometric pressure at 10 m above the sea surface and 100 % humidity at SST and sea surface salinity. Usually, the flask analysis data were satisfactorily comparable to our shipboard measurements of

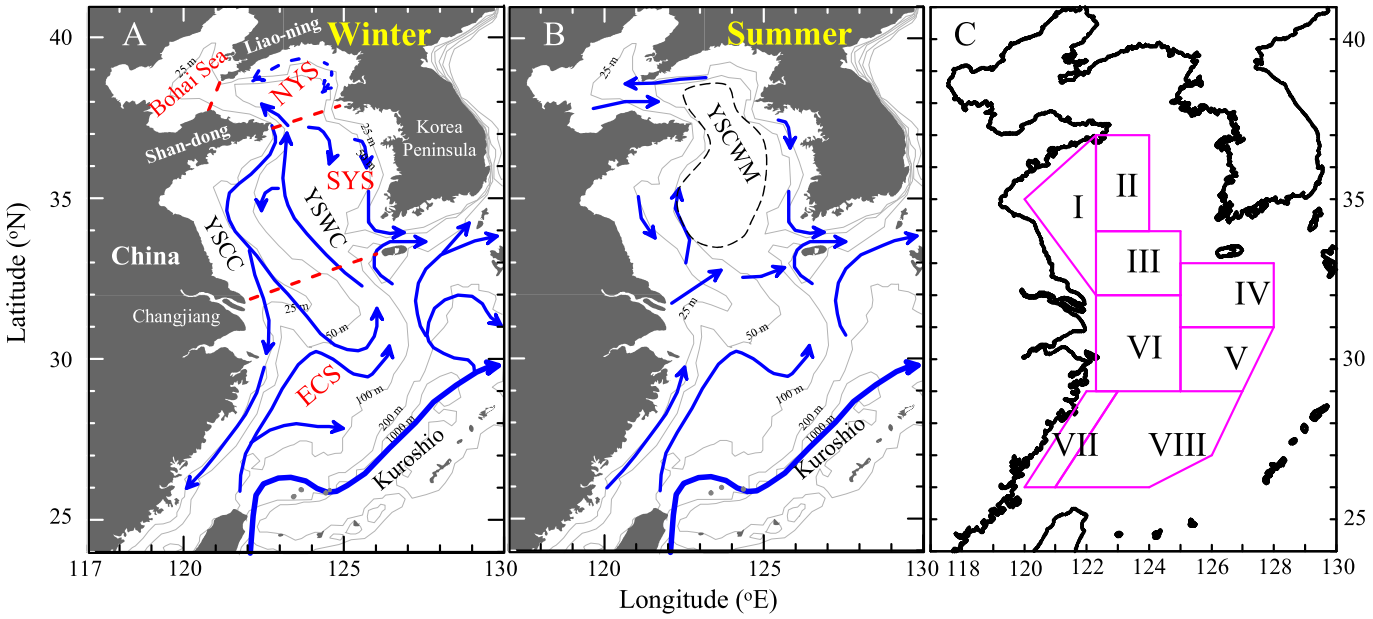

Fig. 1. Area maps. (a) The Bohai Sea, North Yellow Sea (NYS), South Yellow Sea (SYS), East China Sea (ECS), and circulation in winter; (b) circulation in summer (Chen, 2009; Zhai, 2018); and (c) the physical–biogeochemical domains categorized in this study, as detailed in Table 1 (for the SYS) and Table S2 (for the ECS). In panel (a), YSCC = Yellow Sea Coastal Current, and YSWC = Yellow Sea Warm Current. In panel (b), YSCWM = Yellow Sea Cold Water Mass. Depth contours of 25, 50, 100, 200 and 1000 m are shown as thin gray lines; boundaries of sea areas are shown as red dashed lines. (For interpretation of the references to colour in this figure legend, the reader is referred to the web version of this article.)

Table 1
Physical–biogeochemical domains in the South Yellow Sea (SYS) categorized in the present study.

Subregion #	Subregion name / description	Characteristics	Latitude (°N)	Longitude (°E)	Area (10^3 km^2)	Surveying months
I	Western part of the SYS	Shallow waters (<50 m), sediment resuspension	32 – 37	120 – 122.3	58.138	Apr. 2005, May 2005, Sep. 2006, Oct. 2006, Jul. 2007, Nov. 2007, Mar. 2008, Apr. 2008, Aug. 2008, Sep. 2008, Dec. 2008, Jan. 2009, Mar. 2009, Apr. 2009, May 2009, Jun. 2009, Jul. 2009, Aug. 2009, Feb. 2010, Dec. 2010, Apr. 2011, Jun. 2011, Nov. 2011, Dec. 2011
II	Chinese side of the central SYS	Highly stratified in summer, warm current in winter	34 – 37	122.3 – 124	51.330	May 2005, Sep. 2006, Aug. 2008, Mar. 2009, Apr. 2009, May 2009, Jun. 2009, Aug. 2009, Feb. 2010, Jun. 2011, Nov. 2011, Dec. 2011
III	Southern part of the SYS	Highly stratified in summer, with river plume signals visible in flood seasons	32 – 34	122.3 – 125	55.958	Apr. 2005, May 2005, Sep. 2006, Oct. 2006, Nov. 2006, Jul. 2007, Mar. 2008, Apr. 2008, Aug. 2008, Sep. 2008, Mar. 2009, Apr. 2009, May 2009, Jul. 2009, Aug. 2009, Feb. 2010, Dec. 2010, Apr. 2011, Jun. 2011, Dec. 2011

atmospheric xCO$_2$ (Supplementary Fig. S2).

In situ measurements of the k value in the SYS were unavailable, and therefore we calculated the k value using the Sweeney et al. (2007) empirical function of wind speed at 10-m height (u_{10}), which is a modification from Wanninkhof (1992) empirical functions. Notably, the Sweeney et al. (2007) formula has been verified by Takahashi et al. (2009), Ho et al. (2011) and Yang et al. (2022) using their own reanalysis and/or field-measured data. Wanninkhof (2014) also proposed an empirical formula that produces results only ~ 10 % lower than those obtained using the Sweeney et al. (2007) formula. According to Yang et al. (2022) synthesis of air–sea CO$_2$ transfer velocity estimates from ship-based eddy covariance (EC) measurements, estimates of CO$_2$ fluxes obtained using a u_{10}^2 dependence with zero intercept are likely biased when the u_{10} values are < 7 m s^{-1}. They developed an empirical function that produces k values similar to those derived using the Sweeney et al. (2007) parameterization at moderate–high wind speed, but that substantially exceed the latter at low wind speed, possibly attributable in part to chemical enhancement in air–sea CO$_2$ exchange (Wanninkhof and Knox, 1996). In this study, we also calculated the k value based on the Yang et al. (2022) empirical function to compare our results with those considering the effect of chemical enhancement at low wind speed.

Wind speed data with 0.25°×0.25° spatial resolution and daily temporal resolution were obtained from the Cross-Calibrated Multi-Platform (CCMP) Ocean Surface Wind dataset developed by the U.S. Jet Propulsion Laboratory. The data were derived through cross-calibration and assimilation of data from several sensors (i.e., SSM/I, TMI, AMSR-E, SeaWinds on QuikSCAT and SeaWinds on ADEOS-II), which were also combined with conventional observations and a starting estimate of the wind field derived using a variational analysis method. The monthly average was adopted in the calculation of the air–sea CO$_2$ flux.

Following Wanninkhof (1992), the effect of short-term variability in wind speed over a month on the gas transfer velocity was determined using $C2 = (u_j^2)_{mean}/(u_{mean})^2$, where u_j is all of the available satellite-derived near surface wind speeds (units: m s^{-1}) in a month, the subscript "mean" indicates the average, and u_{mean} is the monthly mean wind speed. During our study period, the satellite-derived $C2$ varied between 1.14 and 1.53 (Tables 2–4), similar to the range reported earlier (1.17–1.65) as derived from field data recorded by onboard weather stations (Wang and Zhai, 2021).

The Sweeney et al. (2007) equation (S07 for short) is expressed as follows:

$$k(/\text{cm h}^{-1}) = C2 \times 0.27\, u_{10}^2 \times (\text{Sc}/660)^{-0.5}, \quad (1)$$

while the EC-derived (EC22 for short) equation developed by Yang et al. (2022) is expressed as follows:

$$k(/\text{cm h}^{-1}) = C2 \times (0.36 + 1.203\, u_{10} + 0.167\, u_{10}^2) \times (\text{Sc}/660)^{-0.5}, \quad (2)$$

where u_{10} (unit: m s^{-1}) is the satellite-derived monthly mean near-surface wind speed at 10-m height; $C2$ is the nonlinearity coefficient, assuming that the long-term wind follows a Raleigh (Weibull) distribution (Wanninkhof, 1992); Sc is the Schmidt number of CO$_2$ in seawater; and 660 is the Sc value in seawater at salinity of 35 and temperature of 20°C (Wanninkhof, 1992).

3. Results

3.1. Data overview

Over the SYS, survey-averaged SST varied between 4.2 ± 1.0 °C in the western part (Subregion I) in February 2010 and 27.6 ± 1.0 °C in the southern part (Subregion III) in August 2008 (Fig. 2). In contrast to the substantial seasonal variation in SST, survey-averaged surface salinity usually showed limited variation, ranging between 30.9 ± 0.5 (in November 2007) and 32.1 ± 0.5 (in March 2009) in Subregion I, and from 30.9 ± 0.5 (in August 2008) to 33.2 ± 0.6 (in April 2009) in Subregion II (i.e., the central SYS). In Subregion III, survey-averaged surface salinity exhibited the lowest value of 29.6 ± 1.6 (in July 2009) recorded in this study, and the relatively high value of 33.0 ± 0.7 was recorded in November 2006. The relatively low values of salinity of < 30 and substantial standard deviation of salinity of > 1.0 were observed in late spring and summer (Fig. 2F), indicating the Changjiang Diluted Water in this subregion (Fig. 1B). It is also worth noting that in Subregions I and II, relatively high survey-averaged surface salinity values of 32–33 were usually associated with winter/spring cold waters, while relatively low survey-averaged surface salinity values of 30–31 were usually associated with summertime/autumnal warm waters (Fig. 2).

During the study period, sea surface pCO$_2$ exhibited dramatic heterogeneity, with huge variations in both temporal and spatial spans. In the SYS, the two lowest pCO$_2$ values of ~ 100 μatm (120 μatm at 32°17′N 122°47′E in May 2009 and 88 μatm at 32°01′N 122°40′E in June 2011) and the two highest pCO$_2$ values of ~ 810 μatm (804 μatm at 32°05′N 122°12′E in August 2008 and 818 μatm at 32°29′N 122°42′E in early September 2008) were observed near the Changjiang Estuary. In Subregion I, survey-averaged surface pCO$_2$ varied between 285 ± 16 μatm in February 2010 and 458 ± 55 μatm in June 2011 (Fig. 2G), while survey-averaged surface pCO$_2$ in Subregion II ranged from 298 ± 26 μatm in September 2006 to 374 ± 43 μatm in August 2008 (Fig. 2H). In Subregion III, survey-averaged surface pCO$_2$ usually ranged between 287 ± 66 μatm in July 2007 and 449 ± 83 μatm in October 2006 (Fig. 2I), while the highest survey-averaged value of surface pCO$_2$ of 642 ± 79 μatm was detected in early September 2008.

On the basis of monthly averaged values of the flask analysis data of atmospheric CO$_2$ mole fraction at the Tae-ahn Peninsula site, the air-equilibrated levels of sea surface pCO$_2$ varied between 363 μatm (in Subregion I in August 2009) and 401 μatm (in all of the three subregions

Table 2
Summary of pCO_2, salinity and SST along cruise tracks, and monthly satellite-derived wind speed, and air–sea CO_2 flux estimation in Subregion I, with positive values indicating that the sea area release CO_2 to the atmosphere. The annual air–sea CO_2 flux amounts to -0.9 ± 1.5 mol CO_2 m^{-2} yr^{-1} using S07 equation or -1.0 ± 2.1 mol CO_2 m^{-2} yr^{-1} using EC22 equation (Yang et al., 2022). Note that seasonal average CO_2 fluxes were calculated from the monthly averages of the three calendar months in the given season. Errors in air–sea CO_2 flux estimation are the temporal variability of CO_2 fluxes based on those cruises/surveys.

Observation time	Sea surface pCO_2 (μatm)	Air pCO_2 (μatm)	Salinity	SST (°C)	Wind speed (m s^{-1})	*C2*	Air–sea CO_2 fluxes (mmol CO_2 m^{-2} d^{-1})			
							Survey average (EC22)	Seasonal average (EC22)	Survey average (S07)	Seasonal average (S07)
Dec 2008	336 ± 8 (320–358)	390.2	31.25 ± 0.56 (29.74–32.08)	9.5 ± 1.2 (7.78–11.66)	8.2 ± 3.2	1.14	−11.28	−14.07 ± 7.72 (in winter)	−9.56	−11.11 ± 5.96 (in winter)
Dec 2010	355 ± 18 (319–396)	390.6	31.55 ± 0.13 (31.22–31.79)	12.9 ± 0.5 (11.90–14.09)	8.5 ± 4.2	1.24	−8.19		−7.04	
Dec 2011	400 ± 20 (361–441)	398.7	31.22 ± 0.23 (30.65–31.70)	14.3 ± 0.7 (12.43–15.25)	6.7 ± 3.1	1.21	0.20		0.15	
Jan 2009	313 ± 10 (292–331)	396.3	31.68 ± 0.44 (30.07–32.15)	7.3 ± 1.2 (5.29–8.72)	6.9 ± 4.0	1.32	−15.72		−12.21	
Feb 2010	285 ± 16 (266–320)	398.1	31.88 ± 0.04 (31.73–31.94)	4.2 ± 1.0 (1.84–5.31)	7.0 ± 3.3	1.22	−20.08		−15.63	
Mar 2008	295 ± 24 (225–319)	395.6	32.02 ± 0.43 (31.57–32.88)	7.6 ± 1.1 (6.51–9.46)	4.9 ± 2.2	1.19	−10.46	−4.21 ± 5.57 (in spring)	−6.62	−2.95 ± 3.77 (in spring)
Mar 2009	322 ± 39 (269–398)	391.4	32.07 ± 0.44 (30.90–33.26)	7.4 ± 0.9 (6.05–9.71)	6.7 ± 3.0	1.20	−11.30		−8.63	
Apr 2005	347 ± 19 (313–392)	384.4	31.86 ± 0.22 (31.42–32.47)	7.9 ± 0.8 (6.21–9.10)	4.3 ± 2.5	1.33	–3.66		–2.14	
Apr 2008	371 ± 38 (326–437)	393.3	31.98 ± 0.31 (31.51–32.73)	11.6 ± 1.2 (9.58–13.43)	4.8 ± 3.0	1.37	−2.54		−1.60	
Apr 2009	364 ± 44 (314–444)	393.9	32.07 ± 0.20 (31.57–32.53)	11.1 ± 1.1 (9.69–12.88)	4.8 ± 2.7	1.30	−3.29		−2.06	
Apr 2011	320 ± 17 (270–349)	401.1	32.00 ± 0.19 (31.71–32.45)	8.2 ± 0.5 (7.44–9.20)	5.0 ± 2.6	1.26	−8.99		−5.73	
May 2005	407 ± 29 (363–471)	384.3	31.47 ± 0.60 (28.08–31.82)	13.7 ± 1.7 (11.15–16.57)	4.8 ± 2.8	1.32	2.49		1.56	
May 2009	425 ± 65 (343–619)	386.7	31.16 ± 0.86 (28.62–32.32)	15.1 ± 1.1 (12.61–17.63)	3.9 ± 2.4	1.35	3.24		1.74	
Jun 2009	435 ± 40 (375–642)	375.9	31.57 ± 0.46 (29.75–32.17)	19.4 ± 1.2 (16.31–22.30)	4.4 ± 2.0	1.19	5.09	5.00 ± 4.01 (in summer)	3.00	2.96 ± 2.53 (in summer)
Jun 2011	458 ± 55 (317–609)	386.2	31.47 ± 0.47 (29.98–32.17)	18.6 ± 1.5 (14.88–21.23)	4.9 ± 2.4	1.23	7.28		4.57	
Jul 2007	433 ± 54 (311–564)	370.6	31.11 ± 0.49 (30.50–31.93)	22.7 ± 0.9 (20.14–23.66)	4.0 ± 2.0	1.25	4.86		2.67	
Jul 2009	449 ± 56 (314–507)	367.7	31.13 ± 0.47 (29.66–31.83)	21.9 ± 1.1 (18.54–23.13)	4.6 ± 2.4	1.27	7.79		4.72	
Aug 2008	447 ± 124 (232–804)	374.0	30.30 ± 0.76 (27.36–31.54)	25.7 ± 1.2 (22.40–27.90)	4.5 ± 3.1	1.44	7.74		4.65	
Aug 2009	343 ± 32 (265–381)	366.4	31.10 ± 0.08 (30.93–31.20)	24.7 ± 0.5 (23.85–25.30)	5.6 ± 2.3	1.17	−2.73		−1.87	
Sep 2006	333 ± 14 (313–363)	370.1	31.32 ± 0.11 (31.10–31.63)	22.9 ± 0.2 (22.56–23.43)	5.0 ± 2.9	1.33	−4.11	2.28 ± 5.47 (in autumn)	−2.61	1.77 ± 3.82 (in autumn)
Sep 2008	448 ± 65 (370–573)	382.7	30.42 ± 0.26 (29.87–30.76)	24.1 ± 0.7 (22.53–25.61)	5.7 ± 3.1	1.29	8.50		5.91	
Oct 2006	365 ± 28 (311–459)	378.3	31.04 ± 0.20 (30.55–31.31)	22.6 ± 0.4 (21.93–23.07)	4.9 ± 2.7	1.28	–1.35		−0.85	
Nov 2007	419 ± 20 (376–467)	384.1	30.91 ± 0.49 (29.83–31.44)	18.7 ± 0.3 (18.20–19.77)	6.2 ± 3.0	1.22	5.02		3.68	
Nov 2011	445 ± 22 (421–495)	400.6	31.00 ± 0.12 (30.69–31.12)	16.6 ± 0.5 (15.42–16.92)	6.7 ± 3.2	1.21	6.98		5.32	

in 2011). Through comparison with the air-equilibrated levels of sea surface pCO_2, it was determined that the three subregions of the SYS tended to always absorb CO_2 from the atmosphere in winter, but that the status varied in summer, showing CO_2-degassing in Subregion I, air–sea CO_2 equilibrium in Subregion II, and CO_2-absorbing from the atmosphere in Subregion III (Fig. 2G–I). In spring and autumn, Subregion II was the only area in this study that always served as a CO_2-absorbing region during both transitional seasons, while Subregions I and III tended to release CO_2 to the atmosphere in autumn.

3.2. Air–sea CO_2 fluxes and comparison with those in 2011–2018

The calculated air–sea CO_2 fluxes along the cruise tracks in the three subregions are summarized in Tables 2–4. On the basis of the assumption that these cruise track fluxes were representative of the entire subregions, we obtained an overview of the seasonal variation in air–sea CO_2 exchange over the SYS (Fig. 3). In this study, we used the CCMP wind speed data and the S07 equation (Eq. 1) to calculate the gas transfer velocities, from which we then determined the air–sea CO_2 fluxes. We also calculated the air–sea CO_2 fluxes based on the EC22 equation (Eq. 2) to better quantify the gas transfer velocities and fluxes at relatively low wind speeds. Generally, the two equations produced similar temporal variations, although the EC22 equation sometimes produced relatively large values (Fig. 3).

In the western SYS (i.e., Subregion I), a total of 24 surveys were conducted, spanning 12 calendar months. The survey-averaged air–sea CO_2 fluxes ranged from -15.6 mmol CO_2 m^{-2} d^{-1} in February 2010 to 5.9 mmol CO_2 m^{-2} d^{-1} in early September 2008 (Fig. 3A). In terms of the seasonal average, the air–sea CO_2 fluxes varied from -11.1 ± 6.0 mmol CO_2 m^{-2} d^{-1} in winter and -3.0 ± 3.8 mmol CO_2 m^{-2} d^{-1} in

Table 3
Summary of pCO_2, salinity and SST along cruise tracks, and monthly satellite-derived wind speed, and air–sea CO_2 flux estimation in Subregion II, with positive values indicating that the sea area release CO_2 to the atmosphere. The annual air–sea CO_2 flux amounts to − 1.6 ± 0.5 mol CO_2 m^{-2} yr^{-1} using S07 equation or − 2.3 ± 0.7 mol CO_2 m^{-2} yr^{-1} using EC22 equation (Yang et al., 2022). Note that seasonal average CO_2 fluxes were calculated from the monthly averages of the three calendar months in the given season. Errors in air–sea CO_2 flux estimation are the temporal variability of CO_2 fluxes based on those cruises/surveys.

Observation time	Sea surface pCO_2 (μatm)	Air pCO_2 (μatm)	Salinity	SST (°C)	Wind speed (m s^{-1})	*C2*	Air–sea CO_2 fluxes (mmol CO_2 m^{-2} d^{-1})			
							Survey average (EC22)	Seasonal average (EC22)	Survey average (S07)	Seasonal average (S07)
Dec 2011	363 ± 15 (345–405)	398.6	31.65 ± 0.32 (30.71–32.18)	14.1 ± 0.8 (12.10–15.01)	7.4 ± 3.3	1.20	−6.50	−7.64 ± 1.62 (in winter)	−5.22	−6.14 ± 1.31 (in winter)
Feb 2010	350 ± 20 (310–388)	396.5	32.48 ± 0.46 (31.81–33.80)	8.2 ± 1.7 (4.39–11.67)	7.4 ± 3.4	1.20	−8.78		−7.07	
Mar 2009	347 ± 15 (307–369)	391.0	33.20 ± 0.43 (32.07–33.80)	9.6 ± 0.8 (7.24–10.60)	7.2 ± 3.4	1.22	−7.92	−9.03 ± 3.02 (in spring)	−6.29	−5.97 ± 2.17 (in spring)
Apr 2009	289 ± 23 (255–335)	395.5	33.22 ± 0.56 (32.20–33.78)	11.4 ± 0.7 (10.21–12.23)	4.8 ± 3.2	1.43	−12.73		−7.98	
May 2005	319 ± 15 (293–363)	383.3	32.91 ± 0.33 (31.83–33.39)	13.6 ± 0.7 (12.27–14.94)	4.3 ± 3.2	1.53	−6.97		−4.04	
May 2009	314 ± 39 (277–414)	385.7	32.16 ± 0.56 (31.31–32.94)	13.6 ± 0.8 (10.98–14.92)	4.0 ± 2.2	1.27	−5.89		−3.23	
Jun 2009	366 ± 37 (281–464)	374.9	32.23 ± 0.43 (31.22–33.09)	19.5 ± 1.4 (16.84–22.17)	4.7 ± 2.2	1.22	−0.80	−1.10 ± 1.04 (in summer)	−0.49	−0.70 ± 0.67 (in summer)
Jun 2011	373 ± 24 (331–442)	386.3	32.03 ± 0.47 (30.85–32.84)	18.6 ± 1.8 (12.57–21.47)	4.7 ± 2.8	1.35	−1.37		−0.84	
Aug 2008	374 ± 43 (292–436)	373.0	30.92 ± 0.44 (30.25–31.71)	27.4 ± 0.5 (25.92–28.33)	4.5 ± 2.9	1.39	0.12		0.07	
Aug 2009	344 ± 45 (262–392)	365.2	31.10 ± 0.57 (29.97–31.72)	25.8 ± 0.6 (24.27–26.58)	5.1 ± 2.7	1.26	−2.34		−1.52	
Sep 2006	298 ± 26 (246–325)	370.3	31.07 ± 0.30 (30.49–31.39)	23.5 ± 0.3 (23.08–24.21)	5.2 ± 2.9	1.30	−8.43	−7.28 ± 1.62 (in autumn)	−5.54	−5.10 ± 0.63 (in autumn)
Nov 2011	363 ± 28 (334–432)	401.1	31.30 ± 0.36 (30.74–31.92)	15.1 ± 0.5 (14.15–16.18)	6.7 ± 3.2	1.22	−6.14		−4.66	

spring to 3.0 ± 2.6 mmol CO_2 m^{-2} d^{-1} in summer and 1.8 ± 3.9 mmol CO_2 m^{-2} d^{-1} in autumn (Table 2). The annual air–sea CO_2 flux estimation (−0.9 ± 1.5 mol m^{-2} yr^{-1} using the S07 equation and − 1.0 ± 2.1 mol CO_2 m^{-2} yr^{-1} using the EC22 equation) indicated that this subregion tended to be a weak sink area of atmospheric CO_2, consistent with the earlier estimate over the western SYS (with an annual air–sea CO_2 flux of − 0.2 ± 2.2 mol m^{-2} yr^{-1} using the S07 equation) based on data obtained during 2011–2018 and the same atmospheric CO_2 data set at the Tae-ahn Peninsula site (Wang and Zhai, 2021).

In the central SYS (Subregion II), a total of 12 surveys were conducted, spanning 9 out of 12 calendar months, i.e., excluding January, July and October. The survey-averaged air–sea CO_2 fluxes ranged from − 8.0 mmol CO_2 m^{-2} d^{-1} in late April 2009 to 0.1 mmol CO_2 m^{-2} d^{-1} in August 2008 (Fig. 3B). In terms of the seasonal average, the air–sea CO_2 fluxes varied from − 6.1 ± 1.4 mmol CO_2 m^{-2} d^{-1} in winter and − 6.0 ± 2.2 mmol CO_2 m^{-2} d^{-1} in spring to − 0.7 ± 0.7 mmol CO_2 m^{-2} d^{-1} in summer and − 5.1 ± 0.7 mmol CO_2 m^{-2} d^{-1} in autumn (Table 3). The annual air–sea CO_2 flux estimation (−1.6 ± 0.5 mol m^{-2} yr^{-1} using the S07 equation and − 2.3 ± 0.7 mol CO_2 m^{-2} yr^{-1} using the EC22 equation) indicated that this subregion used to be a stronger CO_2-absorbing area during 2005–2011 compared with the estimate derived by Wang and Zhai (2021) for annual air–sea CO_2 flux over the central SYS (i.e., −0.8 ± 1.8 mol m^{-2} yr^{-1} using the S07 equation based on data obtained during 2011–2018 and the same atmospheric CO_2 data set at the Tae-ahn Peninsula site).

In the southern SYS (i.e., Subregion III), a total of 20 surveys were conducted, spanning 11 out of 12 calendar months, i.e., excluding January. The survey-averaged air–sea CO_2 fluxes ranged from − 8.4 mmol CO_2 m^{-2} d^{-1} in February 2010 to 5.5 mmol CO_2 m^{-2} d^{-1} in October 2006 and 28.0 mmol CO_2 m^{-2} d^{-1} in early September 2008 (Fig. 3C). In terms of the seasonal average, the air–sea CO_2 fluxes varied from − 3.8 ± 5.8 mmol CO_2 m^{-2} d^{-1} in winter and − 3.5 ± 2.7 mmol CO_2 m^{-2} d^{-1} in spring to − 3.9 ± 2.5 mmol CO_2 m^{-2} d^{-1} in summer and 0.8 ± 5.0 mmol CO_2 m^{-2} d^{-1} in autumn (Table 4), ignoring the extremely high value (~28 mmol CO_2 m^{-2} d^{-1}) obtained in September 2008. The annual air–sea CO_2 flux estimation (−0.9 ± 2.3 mol m^{-2} yr^{-1} using the S07 equation or − 1.3 ± 3.1 mol CO_2 m^{-2} yr^{-1} using the EC22 equation) indicated that this subregion also tended to be a CO_2 sink area, comparable to the estimate derived by Wang and Zhai (2021) over the southern SYS (i.e., −0.1 ± 2.0 mol m^{-2} yr^{-1} using the S07 equation based on data obtained during 2011–2018 and the same atmospheric CO_2 data set at the Tae-ahn Peninsula site).

To further compare the seasonal variations in air–sea CO_2 fluxes during the two periods, we manually fitted the monthly variations in air–sea CO_2 fluxes in 2005–2011 based on the data investigated in this study (Fig. 3A–C), and copied the fitting curves to those plots based on data obtained during 2011–2018 (Fig. 3D–F). Although neither the zoning details nor the air–sea CO_2 flux estimates of the two periods were exactly the same, the fitting curves of the monthly variations in Subregions I and II in 2005–2011 were consistent with those of the monthly variations during 2011–2018 (Fig. 3D–E), showing that similar air–sea CO_2 exchanges and seasonal variations occurred during the two periods. In Subregion III, the fitting curve (showing the monthly variation in the air–sea CO_2 flux during 2005–2011) located systematically to one side of those estimated for 2011–2018, indicating that annual CO_2 uptake had weakened in this subregion (Fig. 3F). Even if we could properly integrate the episodic CO_2-release event observed in early September 2008 into the seasonal air–sea CO_2 flux estimation of this subregion, the systematic change between the two periods would not be reversed.

Despite the systematic change revealed in Subregion III, our results suggest that the SYS did not experience a change from being an annually CO_2-degassing area to becoming a CO_2-absorbing area during the two periods. By contrast, it served as a sink for atmospheric CO_2 during both periods. The area-weighted average of the CO_2 influx rate was estimated to be 1.1 ± 1.5 mol m^{-2} yr^{-1} (using the S07 equation) or 1.5 ± 2.0 mol m^{-2} yr^{-1} (using the EC22 equation) over the three subregions during 2005–2011. Given the dynamic and heterogeneous nature of the air–sea CO_2 flux in shelf seas, the new estimate for 2005–2011 was broadly consistent with the value of 0.4 ± 2.1 mol m^{-2} yr^{-1} reported for 2011–2018 (using the S07 equation) based on another SYS dataset

Table 4
Summary of pCO_2, salinity and SST along cruise tracks, and monthly satellite-derived wind speed, and air–sea CO_2 flux estimation in Subregion III, with positive values indicating that the sea area release CO_2 to the atmosphere. The annual air–sea CO_2 flux amounts to -0.9 ± 2.3 mol CO_2 m^{-2} yr^{-1} using S07 equation or -1.3 ± 3.1 mol CO_2 m^{-2} yr^{-1} using EC22 equation (Yang et al., 2022). Note that seasonal average CO_2 fluxes were calculated from the monthly averages of the three calendar months in the given season. Errors in air–sea CO_2 flux estimation are the temporal variability of CO_2 fluxes based on those cruises/surveys. The extremely high value obtained in September 2008 has been removed from the seasonal average and the annual mean flux estimation, while it was involved in the assessment of the temporal variability.

Observation time	Sea surface pCO_2 (μatm)	Air pCO_2 (μatm)	Salinity	SST (°C)	Wind speed (m s^{-1})	*C2*	Air–sea CO_2 fluxes (mmol CO_2 m^{-2} d^{-1})			
							Survey average (EC22)	Seasonal average (EC22)	Survey average (S07)	Seasonal average (S07)
Dec 2010	408 ± 21 (376–451)	393.2	32.29 ± 0.88 (31.08–33.52)	15.6 ± 1.1 (13.79–16.81)	8.7 ± 4.5	1.26	3.57	−4.88 ± 7.12 (in winter)	3.11	−3.81 ± 5.77 (in winter)
Dec 2011	388 ± 19 (349–417)	398.4	31.66 ± 0.18 (31.32–31.98)	15.3 ± 0.7 (14.57–16.64)	7.9 ± 3.4	1.18	−1.98		−1.64	
Feb 2010	337 ± 14 (312–355)	395.6	32.80 ± 0.92 (31.46–34.06)	10.0 ± 1.6 (7.58–12.15)	7.2 ± 3.5	1.22	−10.55		−8.36	
Mar 2008	354 ± 13 (324–371)	392.5	32.51 ± 0.20 (32.19–33.06)	9.3 ± 0.4 (8.75–10.35)	5.9 ± 2.9	1.24	−5.35	−5.20 ± 4.07 (in spring)	−3.78	−3.48 ± 2.64 (in spring)
Mar 2009	359 ± 13 (330–379)	390.4	32.31 ± 0.79 (31.21–33.86)	9.2 ± 0.9 (7.70–10.74)	7.2 ± 3.1	1.18	−5.39		−4.26	
Apr 2005	391 ± 15 (354–419)	385.8	31.74 ± 1.24 (27.65–32.74)	9.2 ± 0.8 (8.53–12.12)	4.5 ± 2.7	1.35	0.51		0.30	
Apr 2008	394 ± 52 (282–443)	394.0	31.67 ± 1.36 (26.99–32.55)	13.2 ± 0.7 (12.29–15.02)	4.8 ± 2.4	1.25	0.04		0.02	
Apr 2009	305 ± 69 (231–440)	395.2	32.00 ± 1.20 (27.92–33.45)	12.3 ± 1.0 (11.33–15.46)	5.2 ± 3.2	1.36	−11.42		−7.52	
Apr 2011	364 ± 60 (189–423)	400.9	32.43 ± 0.29 (31.56–33.07)	9.7 ± 0.9 (8.72–11.96)	5.6 ± 2.7	1.22	−4.63		−3.17	
May 2005	351 ± 59 (214–453)	383.5	31.39 ± 2.30 (26.31–33.47)	15.0 ± 0.8 (13.33–16.39)	4.7 ± 3.0	1.39	−3.61		−2.22	
May 2009	292 ± 81 (120–431)	387.6	30.58 ± 1.32 (27.10–32.83)	16.1 ± 1.2 (13.05–19.05)	4.5 ± 2.3	1.26	−9.08		−5.42	
Jun 2011	323 ± 59 (88–501)	386.0	31.71 ± 0.87 (27.82–32.85)	18.4 ± 0.8 (16.53–19.97)	5.2 ± 2.6	1.24	−6.97	−5.93 ± 3.63 (in summer)	−4.56	−3.89 ± 2.44 (in summer)
Jul 2007	287 ± 66 (165–417)	370.5	31.33 ± 0.80 (28.81–32.32)	23.0 ± 1.1 (21.83–25.05)	4.4 ± 2.3	1.25	−7.45		−4.38	
Jul 2009	374 ± 78 (272–544)	368.2	29.59 ± 1.60 (26.67–31.53)	21.9 ± 0.9 (20.47–23.43)	5.4 ± 2.6	1.22	0.72		0.48	
Aug 2008	308 ± 65 (181–401)	371.7	30.94 ± 0.69 (29.27–32.15)	27.6 ± 1.0 (24.60–29.29)	5.1 ± 2.6	1.26	−6.97		−4.51	
Aug 2009	302 ± 72 (182–463)	363.2	30.25 ± 1.78 (24.92–32.34)	26.7 ± 0.8 (25.22–28.05)	6.2 ± 2.5	1.15	−7.96		−5.81	
Sep 2006	333 ± 57 (252–414)	370.6	31.58 ± 0.72 (30.48–33.10)	23.0 ± 0.9 (21.89–24.33)	6.7 ± 3.1	1.21	−5.77	1.33 ± 19.14 (in autumn)	−4.39	0.82 ± 14.15 (in autumn)
Sep 2008	642 ± 79 (538–818)	381.8	31.21 ± 0.44 (30.49–32.10)	24.3 ± 0.8 (22.23–25.08)	6.3 ± 3.2	1.24	37.87		27.95	
Oct 2006	449 ± 83 (193–580)	377.3	31.82 ± 0.83 (30.84–33.37)	23.4 ± 0.7 (21.96–24.18)	5.4 ± 2.6	1.22	8.17		5.47	
Nov 2006	389 ± 34 (318–456)	381.7	33.02 ± 0.65 (31.54–33.65)	19.4 ± 1.0 (17.11–20.22)	8.8 ± 3.0	1.12	1.58		1.39	

released by Wang and Zhai (2021). At most, the CO_2 influx rate over the SYS might have experienced slight weakening during the two periods.

3.3. Comparing air–sea CO_2 fluxes with the adjacent East China sea

Over the adjacent ECS shelf, using the S07 equation, annual air–sea CO_2 influx rates ranged from 1.7 ± 2.0 mol m^{-2} yr^{-1} in Subregion V to 2.3 ± 1.8 mol m^{-2} yr^{-1} in Subregions IV and VI (Supplementary Tables S3–S7), broadly consistent with the earlier data-based estimates (Zhai and Dai, 2009; Tseng et al., 2014; Guo et al., 2015) and a satellite-based estimate (1.5 ± 1.4 mol m^{-2} yr^{-1} for the entire ECS) released by Yu et al. (2023). In the SYS, the only substantial CO_2-absorbing value was observed in Subregion II (i.e., the central SYS), where the annual air–sea CO_2 influx rate of 1.6 ± 0.5 mol m^{-2} yr^{-1}, estimated using the S07 equation (Table 3), reached the lower limit of the range of annual air–sea CO_2 influx rates in the ECS. The area-weighted average of the CO_2 influx rate over the surveyed areas of the SYS was only half that of the ECS shelf value, indicating again that the Yellow Sea serves as a weak CO_2 absorber among various CO_2-absorbing continental shelf areas (Wang and Zhai, 2021).

4. Discussion

4.1. Factors influencing seasonal variations in sea surface pCO_2

As reported by Guo et al. (2015), surface pCO_2 was highly heterogenous over the SYS and ECS, especially near the Changjiang Estuary. It remains a challenge to better understand the complex influences of spring algal blooms, the summer river plume from Changjiang, the autumnal collapse of coastal zone hypoxia, and the cold coastal current in winter on the seasonal variation in surface pCO_2 over the SYS and ECS (e.g., Zhai and Dai, 2009; Wang and Zhai, 2021). To consider certain evidence, survey-averaged pCO_2 was plotted against SST and salinity (Fig. 4). Except for the cold seasons in Subregion I, the relationship between pCO_2 and SST exhibited no clear pattern, while pCO_2 versus salinity showed a mixture of water mixing (between relatively high pCO_2 at low salinity and relatively low and/or nearly air-equilibrated pCO_2 at high salinity) and likely biological CO_2 drawdown/addition at intermediate salinity.

Subregion-specific seasonal variations in cruise-averaged SST were broadly the same between the two periods (Supplementary Fig. S3), and

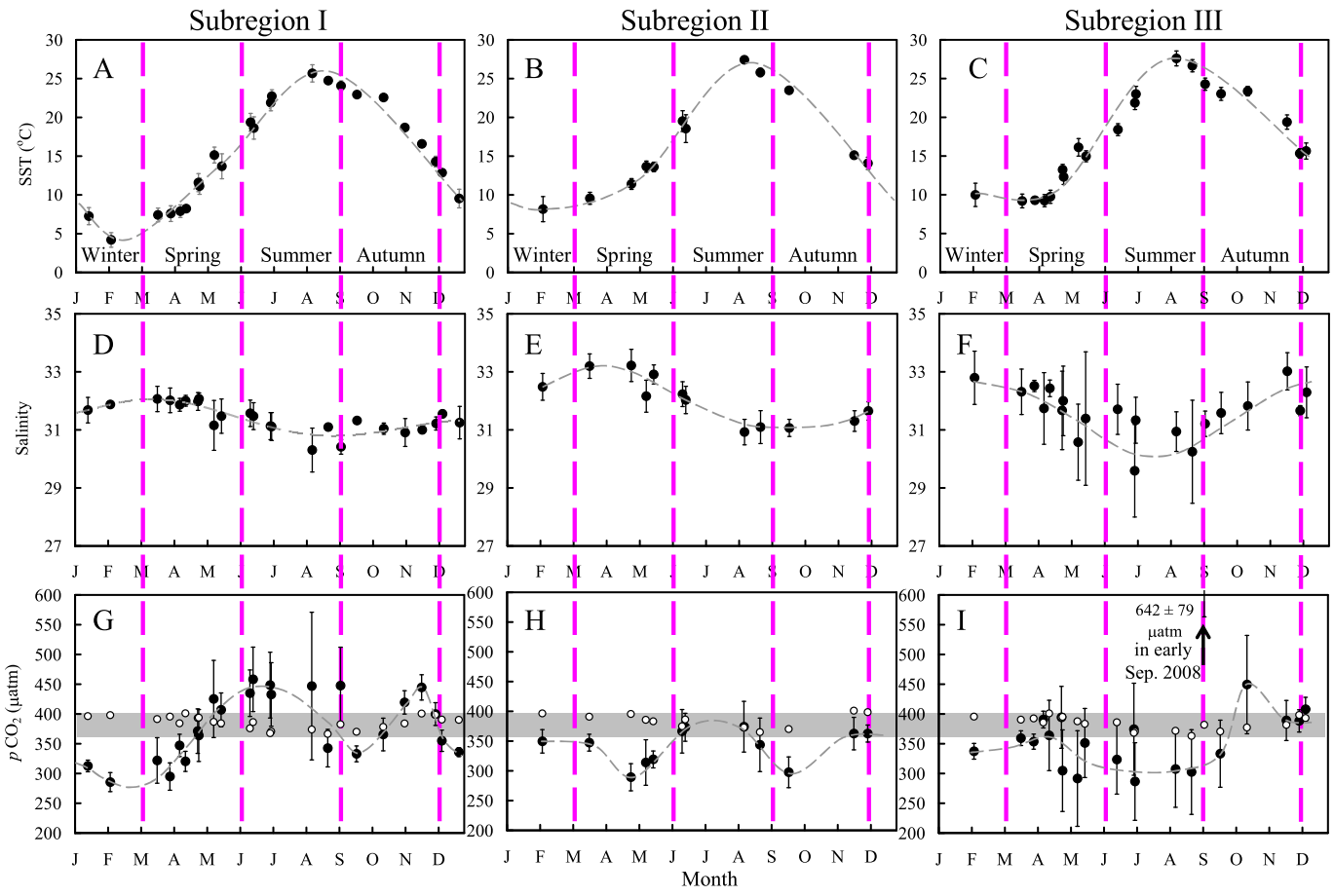

Fig. 2. Seasonal variations in sea surface temperature (SST), salinity and partial pressure of CO_2 (pCO_2) in the three subregions defined in Fig. 1C, and based on data presented in Tables 2–4. Field data are shown as mean ± standard deviation, seasonal breaks are indicated by pink dashed lines, and subregion-specific fitting curves of the monthly variations are manually plotted with dashed curves. In panels G–I, the gray band indicates the range of the air-equilibrated level (open circles) of 360–400 µatm. (For interpretation of the references to colour in this figure legend, the reader is referred to the web version of this article.)

therefore the potential temperature effect on seasonal variations in surface pCO_2 should have behaved similarly during the two periods. The only difference was the relatively high air-equilibrated level of pCO_2 in 2011–2018 (380–420 µatm) compared with that in 2005–2011 (360–400 µatm). To examine this issue, the SST-driven pCO_2 values (pCO_2^{Temp}, unit: µatm) during 2005–2011 were plotted with $pCO_2^{Temp} = (380 \pm 20) \times e^{0.0423\times(SST-mSST)}$, where the value of 380 ± 20 is comparable to the range of the air-equilibrated level of pCO_2 (unit: µatm) at 10-m (Fig. 2G–I), $0.0423°C^{-1}$ is the coefficient for the temperature effect of seawater pCO_2 (Takahashi et al., 1993), and *m*SST is the annual average SST, i.e., 15.46°C in the offshore area of the western SYS (Fig. 4A), 16.20°C in the central SYS (Fig. 4B), and 17.32°C in the southern SYS (Fig. 4C). However, only a few surveys followed the ideal SST-driven lines, implying again that non-thermodynamic regulations of pCO_2 dynamics occurs in this marginal sea (Wang and Zhai, 2021).

To clarify this non-thermodynamic regulation issue, we further calculated the difference between pCO_2 and pCO_2^{Temp}, and plotted it with salinity (Fig. 4G–I). Highly negative values of $pCO_2 - pCO_2^{Temp}$ (with a survey-averaged value of below − 100 µatm) were associated with relatively low salinity of < 31.6 and usually warm waters in the SYS (Fig. 2). Although we have no reliable chlorophyll and/or sufficient DO data to characterize the in situ primary production in this study, the SYS has been widely characterized as having high productivity in the warm seasons (e.g., Guo et al., 2024). Therefore, we contend that these highly negative values of $pCO_2 - pCO_2^{Temp}$ were induced mostly by biological drawdown, especially for those CO_2 uptake cases in the three subregions in the warm seasons (Fig. 4A–C). By contrast, many very high positive values of $pCO_2 - pCO_2^{Temp}$ (with survey-averaged values of usually 40 − 90 µatm) were associated with relatively high survey-averaged salinity of > 31.6 (Fig. 4G–I), with the highest salinity of 33.20 ± 0.43 in Subregion II in March 2009. These very high positive values of $pCO_2 - pCO_2^{Temp}$ were usually recorded in winter and spring (Fig. 5), implying basin-scale pCO_2 addition of 40–90 µatm in the cold seasons, which might be attributable to vertical mixing with CO_2-rich bottom water in the SYS (Zhai, 2018; Wang and Zhai, 2021).

According to Yu et al. (2022), the SYS cold water mass persists in accumulating apparent oxygen utilization and supersaturated CO_2 from spring to late autumn (until December). Even in January, the SYS might still contain some supersaturated CO_2 in the bottom waters (Zhai, 2018). The supersaturated CO_2 can be mixed to surface waters during the ventilation period in late autumn and winter, and it tended to be released into the atmosphere over a temporal scale of 3–4 months (e.g., Zhai et al., 2014). In our dataset, taking Subregion II as an example, the wintertime $pCO_2 - pCO_2^{Temp}$ values (Fig. 4H) increased from 15 ± 15 µatm in December (in 2011) to 79 ± 20 µatm in February (in 2010), and then declined to 60 ± 15 µatm in March (in 2009) and to − 21 ± 23 µatm in April (in 2009). Therefore, the upwelled supersaturated CO_2 counteracted the cooling-induced pCO_2 decline throughout winter, leading to relatively high pCO_2 values in winter when the SST is very low (Fig. 4A–C). Considering horizontal mixing (HM) with the high-salinity Yellow Sea Warm Current in the cold seasons and with the relatively low-salinity Changjiang Diluted Water in the warm seasons (Fig. 1), we proposed a schematic of the non-thermodynamic regulation processes in the SYS (Fig. 4H), involving springtime biological drawdown (BD),

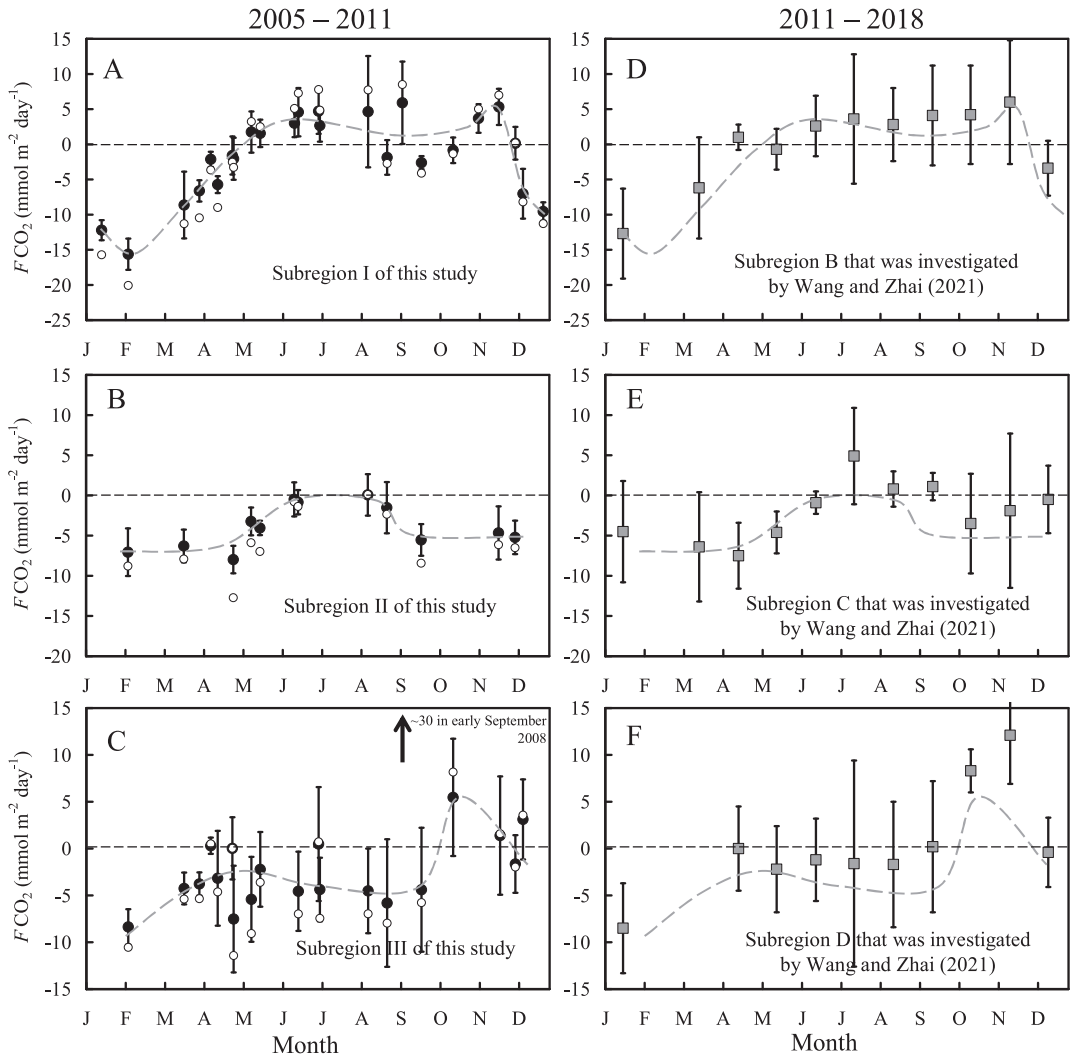

Fig. 3. Seasonal variations in air–sea CO_2 fluxes during 2005–2011 and the comparison with those of 2011–2018. Upper two, middle two, and lower two panels represent the western, central and southern parts of the South Yellow Sea, respectively. In panels (A)–(C), filled circles with error bars denote the flux estimation based on the S07 equation (Eq. 1) for calculating the gas transfer velocity, while open circles without error bars show those flux estimation results based on the EC22 equation (Eq. 2). Errors in air–sea CO_2 flux estimation were based on the spatial variability of surface pCO_2 along those cruise tracks in the given subregion. In panels (A)–(C), dashed curves are manually plotted to show subregion-specific monthly variations in air-sea CO_2 fluxes based on data obtained during 2005–2011. In panels (D)–(F), the dashed curves are exact copies of those in the left-hand column.

autumnal vertical mixing (VM), wintertime VM + HM and summertime BD + HM.

Similar non-thermodynamic regulation of pCO_2 was also identified with survey-averaged $pCO_2 - pCO_2^{Temp}$ values during 2011–2018 (Supplementary Fig. S4). Relevant processes have been discussed using discrete data (Wang and Zhai, 2021). Interestingly, seasonal variations in the survey-averaged $pCO_2 - pCO_2^{Temp}$ values usually exhibited a consistent pattern among the three subregions and during the two periods (Fig. 5), including wintertime CO_2 addition of usually 40 – 90 μatm (through basin-scale vertical mixing during stratification decay in every autumn) and warm-season biological CO_2 drawdown that usually accumulated to a peak of 200–300 μatm in every August (i.e., 279 ± 65 μatm in August 2008, 262 ± 72 μatm in August 2009, and 225 ± 111 μatm in August 2015). In comparison with 2011–2018, the southern SYS (i.e., Subregion III) experienced stronger signals of non-thermodynamic CO_2 drawdown of 35–55 μatm (as indicated by the survey-averaged $pCO_2 - pCO_2^{Temp}$ values) during 2005–2011 (Fig. 5C versus 5F). This might explain the decadal weakening of the air–sea CO_2 flux revealed in Subregion III (Section 3.2), which is discussed further in Section 4.3.

4.2. *Exploring the episodic high sea surface pCO_2 as recorded in early September 2008*

In early September 2008, the highest $pCO_2 - pCO_2^{Temp}$ value of 132 ± 79 μatm of this study was recorded in Subregion III (Fig. 4I), associated with relatively low salinity of 31.21 ± 0.44 and relatively high SST of 24.3 ± 0.8 °C, together with extremely high survey-averaged pCO_2 of 642 ± 79 μatm (Table 4). The high pCO_2 even peaked at 818 μatm, where many unsaturated DO data of ~ 80 % were recorded synchronously (Supplementary Fig. S5). In summer 2008, the SYS attracted public attention owing to a massive green algae bloom (e.g., Liu et al., 2009), which increased the concentration of surface dissolved inorganic carbon (DIC) by 80–100 μmol kg^{-1} during the post-bloom period (Hu et al., 2015). Following Wang and Zhai (2021), this biological addition of DIC could induce an increase in pCO_2 of 228 μatm, i.e., $[\delta DIC/DIC^{avg}] \times RF^{avg} \times pCO_2^{avg} = (100/2100) \times 12 \times 400 = 228$ μatm, where DIC^{avg}, RF^{avg}, and pCO_2^{avg} are regional average values of DIC (~2100 μmol kg^{-1}), the Revelle factor (~12), and pCO_2 (~400 μatm), respectively. Therefore, the post-bloom remineralization could have induced both the high pCO_2 of > 600 μatm and the high $pCO_2 - pCO_2^{Temp}$ value of ~ 200

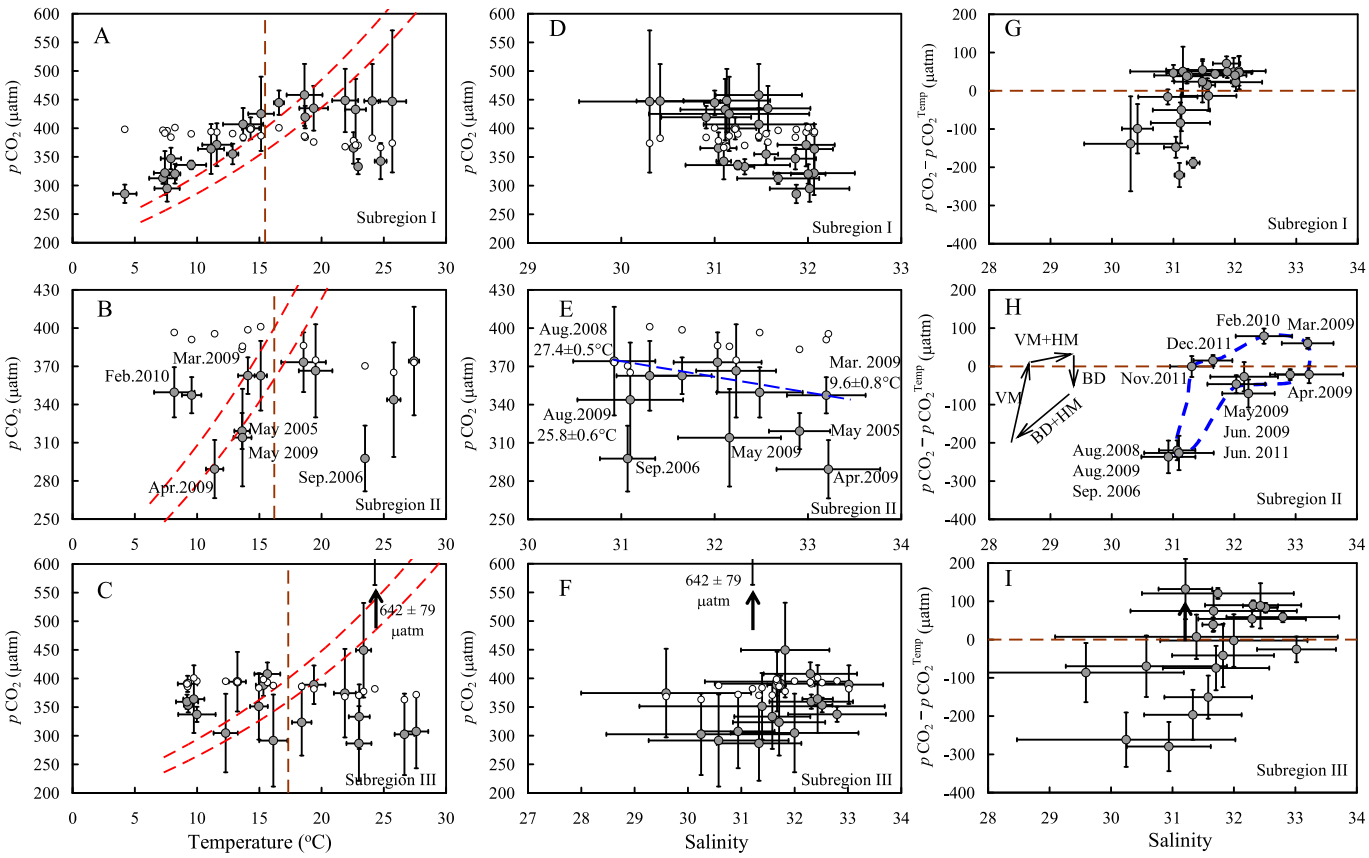

Fig. 4. Cruise-averaged partial pressure of CO_2 (pCO_2) versus sea surface temperature (SST) and salinity (A–F), and the difference in pCO_2 from the SST-driven pCO_2 values ($pCO_2 - pCO_2^{Temp}$) versus salinity (G–I). Upper three, middle three, and lower three panels represent the western, central and southern parts of the South Yellow Sea, respectively. Field data are shown as mean ± standard deviation. Open circles indicate cruise-specific air-equilibrated levels of pCO_2. In panels A-C, red dashed lines show the range of SST-driven pCO_2 values. In panel H, BD = biological drawdown, VM = vertical mixing, and HM = horizontal mixing (with high-salinity Yellow Sea Warm Current in cold seasons and with relatively low-salinity Changjiang Diluted Water in warm seasons). See details in text of Section 4.1. (For interpretation of the references to colour in this figure legend, the reader is referred to the web version of this article.)

µatm over the sea surface. Despite no further observation, this assumption has no contradiction with the field data. By contrast, another potential mechanism (but inapplicable in this case) to explain the unexpected high pCO_2 is the upwelling of subsurface CO_2-rich cold water to the sea surface, which must occur together with salinity increase and water temperature decline that were not evidenced by our data.

Given that summertime green algae blooms have occurred in the SYS annually since 2007 (Xiong et al., 2023), it is puzzling why extremely high pCO_2 was observed only once in our surveys, even including this study (Tables 2–4) and the mapping cruises conducted during 2011–2018 (Wang and Zhai, 2021). To investigate this issue, we considered the air–sea equilibration time $\tau(CO_2)$. Following Zeebe and Wolf-Gladrow (2001) and Zhai et al. (2014), $\tau(CO_2) = d_{ML}/k \times (DIC/[CO_2^*]/RF)$, where d_{ML} is the mixed layer depth (~10 m in summer), k refers to Eqs. (1)–(2) and varies between 2 and 4 m d^{-1}, $DIC/[CO_2^*]$ is the concentration ratio between DIC and free CO_2 (CO_2^*), and RF is the Revelle factor. During calculation, water temperature and salinity were set to 25 °C and 31, respectively (Supplementary Fig. S3), and total alkalinity (TAlk) was set at 2250 µmol kg^{-1} (Zhai, 2018). The calculation program used was CO2SYS.xls (Pelletier et al., 2015), which is an updated version of the original CO2SYS.EXE (Lewis and Wallace, 1998). The dissociation constants for carbonic acid were those determined by Millero et al. (2006), and the dissociation constant for the HSO_4^- ion was determined as per Dickson (1990). The phosphate and silicate concentrations required by the program were replaced by zero.

For the extremely high pCO_2 of 800 µatm, the $DIC:[CO_2^*]$ ratio and the RF were calculated to be 91 and 13.6, respectively, and $\tau(CO_2)$ was estimated at 16–33 d. This $\tau(CO_2)$ value meant that the air–sea disequilibrium of pCO_2 (i.e., 800 – 380 = 420 µatm) declined over 0.5–1.0 months to 37 % (~1/e) of its initial value, and that the observed pCO_2 should be only 380 + 420 × 0.37 = 535 µatm. For the usually high pCO_2 of 450 µatm (Fig. 4), the $DIC:[CO_2^*]$ ratio and the RF were calculated at 154 and 10.7, respectively, and $\tau(CO_2)$ under the same conditions should be 36–72 d. For the usually low pCO_2 of 300 µatm (Fig. 4), the $DIC:[CO_2^*]$ ratio and the RF were calculated to be 222 and 9.2, respectively, and $\tau(CO_2)$ should be 60–120 d. This comparison explains why marine CO_2 uptake events should be observed more often than CO_2 release events. The episodic CO_2 addition reduces the $DIC:[CO_2^*]$ ratio and increases the Revelle factor, thereby diminishing the air–sea equilibration time $\tau(CO_2)$. If the value of $\tau(CO_2)$ was less than 1 month, it would be challenging for researchers to conduct ship-based observation.

In summary, the decomposition of summer green algae blooms might result in temporary sudden increases in seawater pCO_2, leading to rapid CO_2 outgassing that might not be detected through observations. If this interpretation is accurate, the data reported in this study might overestimate the CO_2 absorption capacity of the SYS because the annual decay of green algae blooms is likely to have gone undetected. To fill this gap, volunteer-ship-based and/or mooring-based high-frequency observations might help (e.g., Curbelo-Hernández et al., 2021; Wu et al., 2021).

4.3. On the decadal change in shelf air–sea CO_2 fluxes

It has been speculated that increase in marine pCO_2 in shelf waters

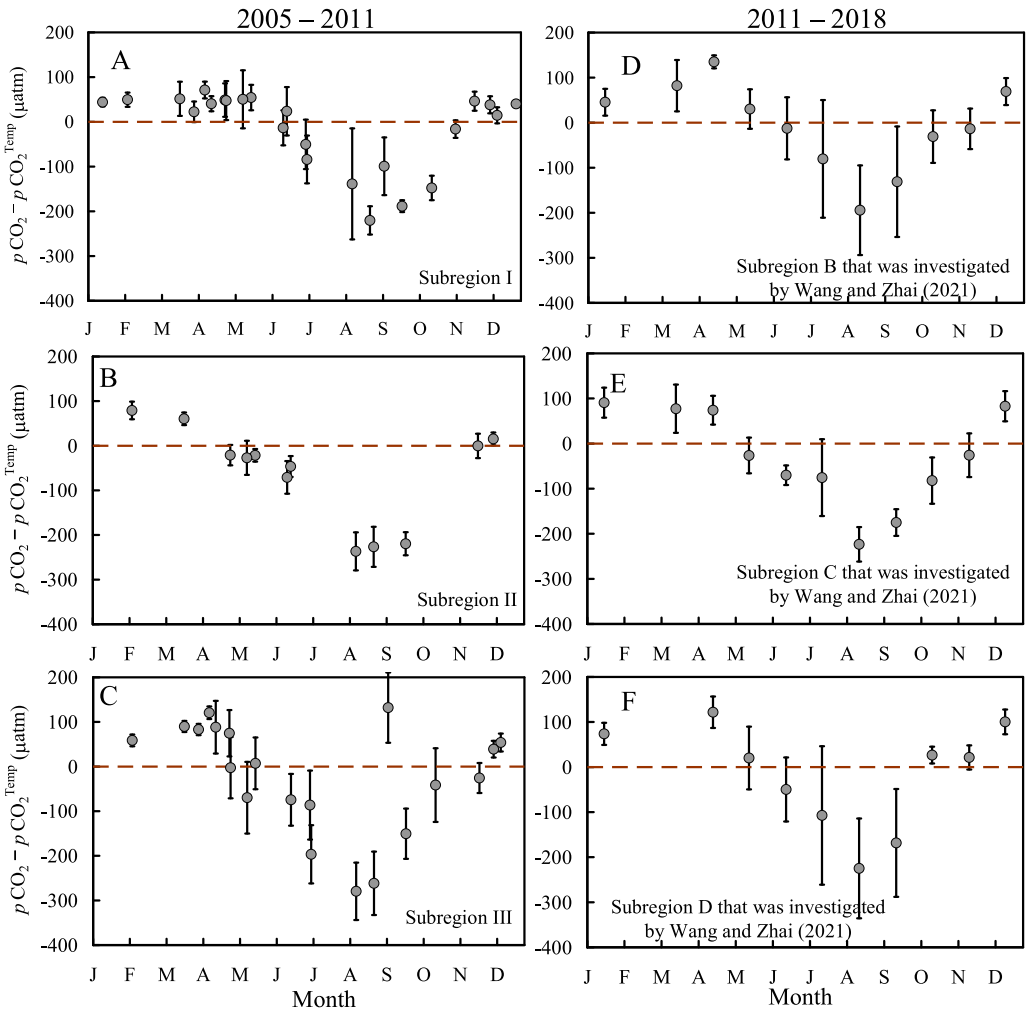

Fig. 5. Seasonal variations in the difference of pCO_2 from SST-driven pCO_2 values and their comparison with those of 2011–2018. Upper two, middle two, and lower two panels show the western, central, and southern parts of the South Yellow Sea, respectively. To calculate the SST-driven pCO_2 values, the annual average of the air-equilibrated level of pCO_2 was fixed at 380 µatm during 2005–2011 and at 400 µatm during 2011–2018.

should follow rise in atmospheric CO_2 with a temporal lag, leading to enhanced CO_2 uptake over some continental shelves (e.g., Laruelle et al., 2018). This hypothesis has been partially proven in the northern South China Sea based on wintertime data of an 18-year dataset (Li et al., 2020). Because the northern South China Sea shelf lies close to slowly-ventilated deep waters, exchange between the surface and deep waters might buffer the effect of atmospheric CO_2 intrusion to a certain extent.

In the SYS, however, water exchange with the adjacent deep ocean is reasonably slow, likely on a scale of several years (Nozaki et al., 1991; Li et al., 2022). Given that the Yellow Sea deep waters are fully ventilated every winter (Zhai, 2018; Yu et al., 2022), annually averaged marine pCO_2 in the Yellow Sea should quickly follow the trend of atmospheric CO_2. Although many other ocean margins (Dai et al., 2022; Mathis et al., 2024) might exhibit different characteristics to those of the Yellow Sea case, the results of this study appear representative for semi-enclosed shallow seas such as the adjacent Bohai Sea (Zhang et al., 2024). Generally, shallow water restricts the potential sequestration and burial of anthropogenic CO_2 on the annual time scale (e.g., Wei et al., 2022), while the limited circulation places restrictions on the horizontal export of anthropogenic CO_2 out of the SYS (Wang and Zhai, 2021).

Considering the counterflow of the wintertime coastal current and the Yellow Sea Warm Current (Fig. 1A) with different TAlk:salinity and DIC:TAlk ratios, this circulation-induced net carbonate export is equivalent to an annual net CO_2 influx rate of approximately 0.7 mol m^{-2} yr^{-1} over the Yellow Sea (Wang and Zhai, 2021). On the basis of sediment samples collected in the 2000 s, the Yellow Sea mean burial flux of total organic carbon has been estimated to be approximately 1.3 mol m^{-2} yr^{-1} (Hu et al., 2016). Both processes are equivalent to a small annual net CO_2 influx rate with magnitude similar to that of our estimates for annual net CO_2 influx in the SYS, suggesting that both circulation-induced net carbonate export and sedimentation of biogenic organic carbon might play a role in maintaining this shelf carbon sink.

For the southern SYS (i.e., Subregion III), the adjacent outer Changjiang Estuary is subject to regional environmental changes. According to Wang et al. (2024), its annual net primary production (NPP) has declined from 280–315 mgC m^{-2} d^{-1} in the 2000 s to 240–260 mgC m^{-2} d^{-1} in the 2010 s, based on a synthesis study combining field incubation for NPP estimation, correction of satellite-derived chlorophyll-a and machine learning. Although this decadal change is consistent with declines in nutrient discharges from the Changjiang River since the early 2010 s (Wang et al., 2023), it has also been attributed primarily to the effect of climate-driven events such as the Pacific Decadal Oscillation and/or the El Niño – Southern Oscillation (Wang et al., 2024). Nevertheless, the decline in the NPP of the outer Changjiang Estuary might also affect the adjacent Subregion III, further inducing potential declines in circulation-induced net carbonate export and sedimentation of biogenic organic carbon. If so, weakening of the annual net air–sea CO_2 influx rate in this subregion (i.e., the slight decline from 0.9 ± 2.3 mol m^{-2} yr^{-1} during 2005–2011 to 0.1 ± 2.0 mol m^{-2} yr^{-1} during 2011–2018) might be related to this regional environmental change.

Considering the reduction in excess nitrogen in the Bohai and Yellow seas in the 2010 s caused by both air pollution control and reduced inflow through rivers (Liang et al., 2023; Wang et al., 2023; Zheng and Zhai, 2023), the slight weakening of the basin-scale annual net air–sea CO_2 influx rate over the SYS in the 2010 s (0.4 ± 2.1 mol m^{-2} yr^{-1} during 2011–2018) compared with that in the 2000 s (1.1 ± 1.5 mol m^{-2} yr^{-1} during 2005–2011) might also be meaningful. According to a modeling study, the present enhancement of coastal ocean CO_2 uptake globally is driven largely by the globally increasing biological carbon fixation (Mathis et al., 2024), as evidenced by satellite-derived phytoplankton bloom dynamics over global coasts during 2003–2020 (e.g., Dai et al., 2023). However, satellite-derived chlorophyll-a over the Bohai and Yellow seas increased before 2011 and declined thereafter (Wang et al., 2021), indicating again that basin-scale eutrophication mitigation occurred in the 2010 s. This is different from many other ocean margins. Therefore, the slight weakening of CO_2-absorbing intensity over the SYS was likely related to eutrophication mitigation and the relevant basin-scale reduction in primary production in the Bohai and Yellow seas, which shares the same logic as Mathis et al. (2024).

Some other factors such as climate-induced changes in open ocean circulation (e.g., Zhang, et al., 2020; Peng et al., 2022; Wang et al., 2022) have severe impact on changes in coastal biogeochemistry and/or air–sea CO_2 flux (e.g., Mathis et al., 2024; Wang et al., 2024). In a given marine system (i.e., the Yellow Sea), it is unclear exactly what would happen following regional environmental changes. Moreover, the uncertainties remain too large to identify changes in the rate of air–sea CO_2 exchange in the Yellow Sea between the 2000 s and 2010 s. Nevertheless, we believe that additional field data should be collected within a certain temporal frame to potentially clarify the changes in CO_2-absorbing intensity in the changing shelf system of the Yellow and the East China seas.

5. Summary and concluding remarks

In this study, we quantified basin-scale air–sea CO_2 exchange flux by resolving both the temporal and the spatial variations in sea surface pCO_2 based on multiple-year underway measurements obtained in the South Yellow Sea (SYS) during 2005–2011. Using the S07 equation, the annual air–sea CO_2 influx rates ranged from 0.9 ± 1.5 mol m^{-2} yr^{-1} in the western SYS (Subregion I) and 0.9 ± 2.3 mol m^{-2} yr^{-1} in the southern SYS (Subregion III) to 1.6 ± 0.5 mol m^{-2} yr^{-1} in the central SYS (Subregion II). The area-weighted average of the CO_2 influx rate was estimated to be 1.1 ± 1.5 mol m^{-2} yr^{-1} over the three subregions under survey during 2005–2011, which was only half that of the value for the East China Sea shelf (ranging from 1.7 ± 2.0 mol m^{-2} yr^{-1} in Subregion V to 2.3 ± 1.8 mol m^{-2} yr^{-1} in Subregions IV and VI).

Over Subregions I and II, both the flux estimation results and the seasonal variation pattern during 2005–2011 were broadly similar to those based on mapping data of discrete fugacity of CO_2, as calculated from DIC and TAlk data obtained in a similar area during 2011–2018. Over Subregion III, however, comparison of the monthly variation in air–sea CO_2 flux during the two periods indicated that the annual CO_2 uptake had weakened in this subregion. Both cases were different from many other ocean margins characterized by enhanced CO_2 uptake following rise in atmospheric CO_2. To study the potential shift from a source to a sink of CO_2 over multiple decades, further field observations and data-based research are needed, especially in relation to large continental shelves that are experiencing environmental changes.

CRediT authorship contribution statement

Wei-dong Zhai: Writing – review & editing, Writing – original draft, Visualization, Validation, Software, Project administration, Methodology, Investigation, Funding acquisition, Formal analysis, Data curation, Conceptualization. **Xiang-hui Guo:** Writing – review & editing, Funding acquisition, Data curation. **Yan Bai:** Resources. **Xianqiang He:** Writing – review & editing, Resources. **Kai Tang:** Writing – review & editing, Funding acquisition. **Minhan Dai:** Resources.

Declaration of competing interest

The authors declare that they have no known competing financial interests or personal relationships that could have appeared to influence the work reported in this paper.

Acknowledgements

We thank Yuancheng Su, Yi Xu, Baoshan Chen, Gui Chen, Qian Li, Hua-de Zhao, and the crew of the *R/V Dongfanghong 2* who provided much help during the sampling surveys. The research was jointly supported by the National Natural Science Foundation of China (grant numbers 92251306, 42141001), the Southern Marine Science and Engineering Guangdong Laboratory (Zhuhai) (project SML2023SP206), the Visiting Fellowship (to Wei-dong Zhai) in the State Key Laboratory of Marine Environmental Science (Xiamen University), and within the context of the Ocean Negative Carbon Emissions (ONCE) Program. We thank three anonymous reviewers for their thoughtful and constructive comments, and James Buxton for editing the English text of a draft of the manuscript, which help us to improve the quality of this paper.

Appendix A. Supplementary data

Supplementary data to this article can be found online at https://doi.org/10.1016/j.pocean.2025.103466.

Data availability

Data will be made available on request.

References

Bauer, J.E., Cai, W.-J., Raymond, P.A., Bianchi, T.S., Hopkinson, C.S., Regnier, P.A.G., 2013. The changing carbon cycle of the coastal ocean. Nature 504, 61–70. https://doi.org/10.1038/nature12857.

Cai, W.-J., 2011. Estuarine and coastal ocean carbon paradox: CO_2 sinks or sites of terrestrial carbon incineration? Ann. Rev. Mar. Sci. 3, 123–145. https://doi.org/10.1146/annurev-marine-120709-142723.

Chen, C.-T.A., Huang, T.-H., Chen, Y.-C., Bai, Y., He, X., Kang, Y., 2013. Air–sea exchanges of CO_2 in the world's coastal seas. Biogeosciences 10 (10), 6509–6544. https://doi.org/10.5194/bg-10-6509-2013.

Chen, C.-T.A., 2009. Chemical and physical fronts in the Bohai, Yellow and east China seas. Journal of Marine System 78 (3), 394–410. https://doi.org/10.1016/j.jmarsys.2008.11.016.

Choi, Y., Kim, D., Cho, S., Kim, T.-W., 2019. Southeastern Yellow Sea as a sink for atmospheric carbon dioxide. Mar. Pollut. Bull. 149, 110550. https://doi.org/10.1016/j.marpolbul.2019.110550.

Curbelo-Hernández, D., Santana-Casiano, J.M., González, A.G., González-Dávila, M., 2021. Air-sea CO_2 exchange in the Strait of Gibraltar. Front. Mar. Sci. 8, 745304. https://doi.org/10.3389/fmars.2021.745304.

Dai, Y.-H., Yang, S.-B., Zhao, D., Hu, C.-M., Xu, W., Anderson, D.M., Li, Y., Song, X.-P., Boyce, D.G., Gibson, L., Zheng, C.-M., Feng, L., 2023. Coastal phytoplankton blooms expand and intensify in the 21st century. Nature 615, 280–284. https://doi.org/10.1038/s41586-023-05760-y.

Dai, M.-H., Su, J.-Z., Zhao, Y.-Y., Hofmann, E.E., Cao, Z.-M., Cai, W.-J., Gan, J.-P., Lacroix, F., Laruelle, G.G., Meng, F.-F., Müller, J.D., Regnier, P.A.G., Wang, G.-Z., Wang, Z.-X., 2022. Carbon fluxes in the coastal ocean: Synthesis, boundary processes and future trends. Annu. Rev. Earth Planet. Sci. 50, 593–626. https://doi.org/10.1146/annurev-earth-032320-090746.

Dai, M.-H., Cao, Z.-M., Guo, X.-H., Zhai, W.-D., Liu, Z.-Y., Yin, Z.-Q., Xu, Y.-P., Gan, J.-P., Hu, J.-Y., Du, C.-J., 2013. Why are some marginal seas sources of atmospheric CO_2? Geophys. Res. Lett. 40 (10), 2154–2158. https://doi.org/10.1002/grl.50390.

Dickson, A.G., 1990. Standard potential of the reaction: AgCl(s)+1/2H_2(g)=Ag(s)+HCl (aq), and the standard acidity constant of the ion HSO_4^- in synthetic sea water from 273.15 to 318.15 K. J. Chem. Thermodyn. 22, 113–127. https://doi.org/10.1016/0021-9614(90)90074-Z.

Guo, S.-J., Sun, X.-X., Zhang, J., Yao, Q.-Z., Wei, C.-J., Wang, F., 2024. Unveiling the evolution of phytoplankton communities: Decades-long insights into the southern Yellow Sea, China (1959–2023). Mar. Pollut. Bull. 201, 116179. https://doi.org/10.1016/j.marpolbul.2024.116179.

Guo, X.-H., Zhai, W.-D., Dai, M.-H., Zhang, C., Bai, Y., Xu, Y., Li, Q., Wang, G.-Z., 2015. Air–sea CO_2 fluxes in the East China Sea based on multiple-year underway

observations. Biogeosciences 12 (18), 5495–5514. https://doi.org/10.5194/bg-12-5495-2015.
Ho, D.T., Wanninkhof, R., Schlosser, P., Ullman, D.S., Hebert, D., Sullivan, K.F., 2011. Toward a universal relationship between wind speed and gas exchange: gas transfer velocities measured with $^3He/SF_6$ during the Southern Ocean Gas Exchange Experiment. J. Geophys. Res. 116, C00F04. https://doi.org/10.1029/2010JC006854.
Hu, Y.-B., Liu, C.-Y., Yang, G.-P., Zhang, H.-H., 2015. The response of the carbonate system to a green algal bloom during the post-bloom period in the southern Yellow Sea. Cont. Shelf Res. 94, 1–7. https://doi.org/10.1016/j.csr.2014.12.006.
Hu, L.-M., Shi, X.-F., Bai, Y.-Z., Qiao, S.-Q., Li, L., Yu, Y.-G., Yang, G., Ma, D.-Y., Guo, Z.-G., 2016. Recent organic carbon sequestration in the shelf sediments of the Bohai Sea and Yellow Sea, China. J. Mar. Syst. 155, 50–58. https://doi.org/10.1016/j.jmarsys.2015.10.018.
Ko, Y.H., Seok, M.-W., Jeong, J.-Y., Noh, J.-H., Jeong, J., Mo, A., Kim, T.-W., 2022. Monthly and seasonal variations in the surface carbonate system and air–sea CO_2 flux of the Yellow Sea. Mar. Pollut. Bull. 181, 113822. https://doi.org/10.1016/j.marpolbul.2022.113822.
Laruelle, G.G., Cai, W.-J., Hu, X.-P., Gruber, N., Mackenzie, F.T., Regnier, P., 2018. Continental shelves as a variable but increasing global sink for atmospheric carbon dioxide. Nat. Commun. 9, 454. https://doi.org/10.1038/s41467-017-02738-z.
Laruelle, G.G., Lauerwald, R., Pfeil, B., Regnier, P., 2014. Regionalized global budget of the CO_2 exchange at the air-water interface in continental shelf seas. Global Biogeochem. Cycles 28, 1199–1214. https://doi.org/10.1002/2014GB004832.
Laruelle, G.G., Dürr, H.H., Slomp, C.P., Borges, A.V., 2010. Evaluation of sinks and sources of CO_2 in the global coastal ocean using a spatially-explicit typology of estuaries and continental shelves. Geophys. Res. Lett. 37, L15607. https://doi.org/10.1029/2010GL043691.
Lewis, E., Wallace, D.W.R., 1998. Program developed for CO_2 system calculations. ORNL/CDIAC-105, Carbon Dioxide Information Analysis Center, Oak Ridge National Laboratory, US Department of Energy, Oak Ridge, Tennessee. doi: 10.2172/639712.
Li, Y.-X., Xue, L., Yang, X.-F., Wei, Q.-S., Xin, M., Xue, M., Han, C.-H., Han, P., Liu, X.-Y., Zang, H., Yang, P.-J., Ran, X.-B., Cao, L., Cai, W.-J., Zhang, L.-J., 2023a. Wastewater inputs reduce the CO_2 uptake by coastal oceans. Sci. Total Environ. 901, 165700. https://doi.org/10.1016/j.scitotenv.2023.165700.
Li, W., Liu, C.-L., Zhai, W.-D., Liu, H.-Z., Ma, W.-J., 2023b. Remote sensing and machine learning method supported sea surface pCO_2 estimation in the Yellow Sea. Front. Mar. Sci. 10, 1181095. https://doi.org/10.3389/fmars.2023.1181095.
Li, C.-L., Yang, D.-Z., Zhai, W.-D., 2022. Effects of warming, eutrophication and climate variability on acidification of the seasonally stratified North Yellow Sea over the past 40 years. Sci. Total Environ. 815, 152935. https://doi.org/10.1016/j.scitotenv.2022.152935.
Li, Q., Guo, X.-H., Zhai, W.-D., Xu, Y., Dai, M.-H., 2020. Partial pressure of CO_2 and air–sea CO_2 fluxes in the South China Sea: Synthesis of an 18-year dataset. Prog. Oceanogr. 182, 102272. https://doi.org/10.1016/j.pocean.2020.102272.
Liang, W., Wang, Y., Mu, J.-L., Wu, N., Wang, J.-Y., Liu, S.-M., 2023. Nutrient changes in the Bohai Sea over the past two decades. Sci. Total Environ. 903, 166696. https://doi.org/10.1016/j.scitotenv.2023.166696.
Liu, D.-Y., Keesing, J.K., Xing, Q.-G., Shi, P., 2009. World's largest macroalgal bloom caused by expansion of seaweed aquaculture in China. Mar. Pollut. Bull. 58 (6), 888–895. https://doi.org/10.1016/j.marpolbul.2009.01.013.
Mathis, M., Lacroix, F., Hagemann, S., Nielsen, D.M., Ilyina, T., Schrum, C., 2024. Enhanced CO_2 uptake of the coastal ocean is dominated by biological carbon fixation. Nat. Clim. Chang. 14, 373–379. https://doi.org/10.1038/s41558-024-01956-w.
Millero, F.J., Graham, T.B., Huang, F., Bustos-Serrano, H., Pierrot, D., 2006. Dissociation constants of carbonic acid in seawater as a function of salinity and temperature. Mar. Chem. 100, 80–94. https://doi.org/10.1016/j.marchem.2005.12.001.
Nozaki, Y., Tsubota, H., Kasemsupaya, V., Yashima, M., Ikuta, N., 1991. Residence times of surface water and particle-reactive ^{210}Pb and ^{210}Po in the East China and Yellow seas. Geochim. Cosmochim. Acta 55 (5), 1265–1272. https://doi.org/10.1016/0016-7037(91)90305-O.
Pelletier, G.J., Lewis, E., Wallace, D.W.R., 2015. CO2SYS.XLS: A Calculator for the CO_2 System in Seawater for Microsoft Excel/VBA, Version 24. Washington State Department of Ecology, Olympia, Washington.
Peng, Q.-H., Xie, S.-P., Wang, D.-X., Huang, R.-X., Chen, G.-X., Shu, Y.-Q., Shi, J.-R., Liu, W., 2022. Surface warming-induced global acceleration of upper ocean currents. Sci. Adv. 8, eabj8394. https://doi.org/10.1126/sciadv.abj8394.
Regnier, P., Friedlingstein, P., Ciais, P., Mackenzie, F.T., Gruber, N., Janssens, I.A., Laruelle, G.G., Lauerwald, R., Luyssaert, S., Andersson, A.J., Arndt, S., Arnosti, C., Borges, A.V., Dale, A.W., Gallego-Sala, A., Goddéris, Y., Goossens, N., Hartmann, J., Heinze, C., Ilyina, T., Joos, F., LaRowe, D.E., Leifeld, J., Meysman, F.J.R., Munhoven, G., Raymond, P.A., Spahni, R., Suntharalingam, P., Thullner, M., 2013. Anthropogenic perturbation of the carbon fluxes from land to ocean. Nat. Geosci. 6 (8), 597–607. https://doi.org/10.1038/NGEO1830.
Resplandy, L., Hogikyan, A., Müller, J.D., Najjar, R.G., Bange, H.W., Bianchi, D., Weber, T., Cai, W.-J., Doney, S.C., Fennel, K., Gehlen, M., Hauck, J., Lacroix, F., Landschützer, P., Le Quéré, C., Roobaert, A., Schwinger, J., Berthet, S., Bopp, L., Chau, T.T.T., Dai, M., Gruber, N., Ilyina, T., Kock, A., Manizza, M., Lachkar, Z., Laruelle, G.G., Liao, E., Lima, I.D., Nissen, C., Rödenbeck, C., Séférian, R., Toyama, K., Tsujino, H., Regnier, P., 2024. A synthesis of global coastal ocean greenhouse gas fluxes. Global Biogeochem. Cycles 38 (1), e2023GB007803. https://doi.org/10.1029/2023GB007803.
Sweeney, C., Gloor, E., Jacobson, A.R., Key, R.M., McKinley, G., Sarmiento, J.L., Wanninkhof, R., 2007. Constraining global air–sea gas exchange for CO_2 with recent bomb ^{14}C measurements. Global Biogeochem. Cycles 21, GB2015. https://doi.org/10.1029/2006GB002784.
Takahashi, T., Sutherland, S.C., Wanninkhof, R., Sweeney, C., Feely, R.A., Chipman, D.W., Hales, B., Friederich, G., Chavez, F., Sabine, C., Watson, A., Bakker, D.C.E., Schuster, U., Metzl, N., Yoshikawa-Inoue, H., Ishii, M., Midorikawa, T., Nojiri, Y., Körtzinger, A., Steinhoff, T., Hoppema, M., Olafsson, J., Arnarson, T.S., Tilbrook, B., Johannessen, T., Olsen, A., Bellerby, R., Wong, C.S., Delille, B., Bates, N.R., de Baar, H.J.W., 2009. Climatological mean and decadal change in surface ocean pCO_2, and net sea–air CO_2 flux over the global oceans. Deep Sea Res. Part II 56, 554–577. https://doi.org/10.1016/j.dsr2.2008.12.009.
Takahashi, T., Olafsson, J., Goddard, J.G., Chipman, D.W., Sutherland, S.G., 1993. Seasonal variation of CO_2 and nutrients in the high-latitude surface oceans: A comparative study. Global Biogeochem. Cycles 7, 843–878. https://doi.org/10.1029/93GB02263.
Tseng, C.-M., Shen, P.-Y., Liu, K.-K., 2014. Synthesis of observed air–sea CO_2 exchange fluxes in the river-dominated East China Sea and improved estimates of annual and seasonal net mean fluxes. Biogeosciences 11 (14), 3855–3870. https://doi.org/10.5194/bg-11-3855-2014.
Tsunogai, S., Watanabe, S., Sato, T., 1999. Is there a "continental shelf pump" for the absorption of atmospheric CO_2? Tellus B Chem. Phys. Meteorol. 51 (3), 701–712. https://doi.org/10.3402/tellusb:v51i3.16468.
Wang, M.-R., Sun, K., Jia, J.-J., Wu, F., Gao, Y., 2024. Climate change drove the decline in Yangtze Estuary net primary production over the past two decades. Environ. Sci. Tech. 58 (43), 19305–19314. https://doi.org/10.1021/acs.est.4c07163.
Wang, Y., Gao, L., Ming, Y., Zhao, L.-B., 2023. Recent declines in nutrient concentrations and fluxes in the lower Changjiang River. Estuar. Coasts 46, 1475–1493. https://doi.org/10.1007/s12237-023-01216-8.
Wang, G.-H., Wu, L.-W., Mei, W., Xie, S.-P., 2022. Ocean currents show global intensification of weak tropical cyclones. Nature 611, 496–500. https://doi.org/10.1038/s41586-022-05326-4.
Wang, S.-Y., Zhai, W.-D., 2021. Regional differences in seasonal variation of air–sea CO_2 exchange in the Yellow Sea. Cont. Shelf Res. 218, 104393. https://doi.org/10.1016/j.csr.2021.104393.
Wang, Y.-Q., Tian, X.-P., Gao, Z.-Q., 2021. Evolution of satellite derived chlorophyll-a trends in the Bohai and Yellow Seas during 2002–2018: Comparison between linear and nonlinear trends. Estuar. Coast. Shelf Sci. 259, 107449. https://doi.org/10.1016/j.ecss.2021.107449.
Wanninkhof, R., 2014. Relationship between wind speed and gas exchange over the ocean revisited. Limnol. Oceanogr. Methods 12, 351–362. https://doi.org/10.4319/lom.2014.12.351.
Wanninkhof, R., Park, G.-H., Takahashi, T., Sweeney, C., Feely, R., Nojiri, Y., Gruber, N., Doney, S.C., McKinley, G.A., Lenton, A., Le Quéré, C., Heinze, C., Schwinger, J., Graven, H., Khatiwala, S., 2013. Global ocean carbon uptake: magnitude, variability and trends. Biogeosciences 10 (3), 1983–2000. https://doi.org/10.5194/bg-10-1983-2013.
Wanninkhof, R., Knox, M., 1996. Chemical enhancement of CO_2 exchange in natural waters. Limnol. Oceanogr. 41 (4), 689–697. https://doi.org/10.4319/lo.1996.41.4.0689.
Wanninkhof, R., 1992. Relationship between wind speed and gas exchange over the ocean. J. Geophys. Res. 97, 7373–7382. https://doi.org/10.1029/92JC00188.
Wei, L., Cai, P.-H., Shi, X.-M., Cai, W.-J., Liu, W., Hong, Q.-Q., Wu, T., Bai, Y., Cheng, P., Sun, Z.-Y., 2022. Winter mixing accelerates decomposition of sedimentary organic carbon in seasonally hypoxic coastal seas. Geochim. Cosmochim. Acta 317, 457–471. https://doi.org/10.1016/j.gca.2021.11.003.
Weiss, R.F., Price, R.A., 1980. Nitrous oxide solubility in water and seawater. Mar. Chem. 8, 347–359. https://doi.org/10.1016/0304-4203(80)90024-9.
Weiss, R.F., 1974. Carbon dioxide in water and seawater: the solubility of a non-ideal gas. Mar. Chem. 2, 203–215. https://doi.org/10.1016/0304-4203(74)90015-2.
Wu, Y.-X., Dai, M.-H., Guo, X.-H., Chen, J.-S., Xu, Y., Dong, X., Dai, J.-W., Zhang, Z.-R., 2021. High-frequency time-series autonomous observations of sea surface pCO_2 and pH. Limnol. Oceanogr. 66 (3), 588–606. https://doi.org/10.1002/lno.11625.
Xiong, T.-Q., Li, H.-M., Yue, Y.-F., Hu, Y.-B., Zhai, W.-D., Xue, L., Jiao, N.-Z., Zhang, Y.-Y., 2023. Legacy effects of late macroalgal blooms on dissolved inorganic carbon pool through alkalinity enhancement in coastal ocean. Environ. Sci. Tech. 57 (5), 2186–2196. https://doi.org/10.1021/acs.est.2c09261.
Yang, M., Bell, T.G., Bidlot, J.-R., Blomquist, B.W., Butterworth, B.J., Dong, Y.-X., Fairall, C.W., Landwehr, S., Marandino, C.A., Miller, S.D., Saltzman, E.S., Zavarsky, A., 2022. Global synthesis of air-sea CO_2 transfer velocity estimates from ship-based eddy covariance measurements. Front. Mar. Sci. 9, 826421. https://doi.org/10.3389/fmars.2022.826421.
Yu, S.-J., Song, Z.-G., Bai, Y., Guo, X.-H., He, X.-Q., Zhai, W.-D., Zhao, H.-D., Dai, M.-H., 2023. Satellite-estimated air-sea CO_2 fluxes in the Bohai Sea, Yellow Sea, and East China Sea: Patterns and variations during 2003–2019. Sci. Total Environ. 904, 166804. https://doi.org/10.1016/j.scitotenv.2023.166804.
Yu, S.-Q., Xiong, T.-Q., Zhai, W.-D., 2022. Quasi-synchronous accumulation of apparent oxygen utilization and inorganic carbon in the South Yellow Sea cold water mass from spring to autumn: The acidification effect and roles of community metabolic processes, water mixing, and spring thermal state. Front. Mar. Sci. 9, 858871. https://doi.org/10.3389/fmars.2022.858871.
Zeebe, R.E., Wolf-Gladrow, D., 2001. Chapter 1 Equilibrium. In: Zeebe, R.E., Wolf-Gladrow, D. (Eds), CO_2 in Seawater: Equilibrium, Kinetics, Isotopes. Elsevier Oceanography Series No. 65, 1–84. doi: 10.1016/S0422-9894(01)80002-7.
Zhai, W.-D., 2018. Exploring seasonal acidification in the Yellow Sea. Sci. China Earth Sci. 61 (6), 647–658. https://doi.org/10.1007/s11430-017-9151-4.
Zhai, W.-D., Zheng, N., Huo, C., Xu, Y., Zhao, H.-D., Li, Y.-W., Zang, K.-P., Wang, J.-Y., Xu, X.-M., 2014. Subsurface pH and carbonate saturation state of aragonite on the

Chinese side of the North Yellow Sea: seasonal variations and controls. Biogeosciences 11 (4), 1103–1123. https://doi.org/10.5194/bg-11-1103-2014.

Zhai, W.-D., Dai, M.-H., 2009. On the seasonal variation of air–sea CO_2 fluxes in the outer Changjiang (Yangtze River) Estuary, East China Sea. Mar. Chem. 117, 2–10. https://doi.org/10.1016/j.marchem.2009.02.008.

Zhang, H.-S., Zhai, W.-D., Tang, K., 2024. Seasonal variations in air-sea CO_2 flux in the Bohai Sea and the temporal relationship between surface and bottom-water carbonate dynamics in a year. Cont. Shelf Res. 275, 105192. https://doi.org/10.1016/j.csr.2024.105192.

Zhang, Y., Zhang, Z.-G., Chen, D.-K., Qiu, B., Wang, W., 2020. Strengthening of the Kuroshio current by intensifying tropical cyclones. Science 368, 988–993. https://doi.org/10.1126/science:aax5758.

Zhang, Y.-H., Huang, Z.-Q., Ma, L.-M., Qiao, R., Zhang, B., 1997. Carbon dioxide in surface water and its flux in East China Sea (in Chinese). Journal of Oceanography in Taiwan Strait 16 (1), 37–42.

Zheng, L.-W., Zhai, W.-D., 2023. Nutrient dynamics in the Bohai and North Yellow seas from seasonal to decadal scales: Unveiling Bohai Sea eutrophication mitigation in the 2010s. Sci. Total Environ. 905, 167417. https://doi.org/10.1016/j.scitotenv.2023.167417.